Politecnico di Torino
Department of Electronics and Telecommunications
Master in Micro and Nanotecnologies for ICTs

Mimicking the Glioblastoma Microenvironment with an *In Vitro* Hydrogel Platform

Master Thesis

Submitted by:
Mariangela Miccoli

Supervisor(s):
Prof. Dr. Janos Vörös,
Dr. Christina Myra Tringides
M.Sc. Giulia Amos
In collaboration with:
Prof. Dr. Tomaso Zambelli
M.Sc. Giacomo Paccagnan
Relator: Prof. Dr. Matteo Cocuzza
Laboratory of Biosensors and Bioelectronics
ETH Zurich

Zurich, August 2024

Preface

enjoy the butterflies, enjoy being naive,
enjoy the nerves, the pressure,
if you want to stand on the top from day one,
then there's nothing else to look forward to,
enjoy the process of making a name for yourself,
and meeting some great people along the way,
a lot of worldly people you can laugh with, learn from,
embrace the good ones, stay focused, don't be too far off your path,
keep trying to build and grow and learn from yourself,
but don't forget what you've got here and bring friends along, bring family along.

- Daniel Ricciardo

Acknowledgment

This work would not have been possible without the support of many individuals to whom I am deeply grateful. First and foremost, I would like to express my sincere thanks to my supervisors, Christina and Giulia, for giving me the chance to work on a project I had long dreamed of. Their guidance and encouragement have been invaluable, while also allowing me the freedom to explore and develop my ideas. I am especially grateful to Giacomo, whose collaboration and friendship have been essential throughout this journey.
I am also fortunate to have had the support of my wonderful office colleagues, Claire, Hanna, and Luc, who made our lab environment enjoyable. Together, we tackled challenges, supported each other, and made lasting memories. A special thanks goes to Luc, who has been not just a friend but also an exceptional mentor. His readiness to help and his dedication have been a significant source of inspiration.

I would also like to extend my heartfelt gratitude to my summer internship supervisor, Francesca, who first introduced me to the intriguing world of material science. Her mentorship allowed me to gain a wealth of knowledge quickly, and her influence has greatly shaped my academic journey.

Additionally, I am deeply thankful for my university friends. Vale, you have always looked out for me, trying to understand my choices, even when I had a hard time explaining them. Your patience and support have meant the world. Vero, your silences often say more than words ever could, and I'm really grateful for the understanding we share. Thank you for your sensitivity, your humor, and all the unforgettable nights and adventures we've had together. Marialucia, our friendship has had more twists and turns than a rollercoaster, but I wouldn't change a single moment. No matter what life throws our way, we always find our way back to a happy ending.
Chiara, your kindness and warm-heartedness throughout this journey have made it all the better.

Finally, I want to express my deepest appreciation to my family, my parents and my sister.
Giulia, thank you for being such a steadfast source of support and a big sister figure throughout this journey, even though you're the youngest. I am incredibly grateful for your constant presence and your willingness to help at any hour, day or night. I may not say it often enough, but your unwavering support and encouragement have meant the world to me. Your kindness and compassion have profoundly impacted my life, and I truly don't know where I would be without you.

To my parents, thank you for being a constant source of strength, even from afar. You have stood by me in every decision, understood the demands of my work, and celebrated every achievement, big or small, with immense love and pride. Your unwavering belief in me has been a cornerstone of my success, and for that, I am truly grateful.

Abstract

In the realm of biomedical research, hydrogels have emerged as a crucial tool. Recent advancements in their production have unlocked the ability to precisely control their mechanical properties, making them invaluable for replicating both healthy and diseased neural tissues. This has paved the way for the development of in vitro models that faithfully mimic the natural extracellular matrix, revolutionizing our ability to culture a wide variety of cells, including the notoriously elusive glioblastoma cancer cells. Glioblastoma, known for its highly invasive nature and formidable treatment challenges, stands as the most lethal form of brain tumor today. Its remarkable intratumor and intertumor heterogeneity presents unparalleled obstacles. Therefore, the development of a 3D in vitro model that accurately mirrors cell-to-cell and cell-to-extracellular matrix interactions is paramount in unraveling the complexities of this enigmatic brain tumor. This project summarizes how matrix stiffness can affect cancer and neuron growth, cell differentiation, migration motility, proliferation, and phenotype.

Keywords: glioblastoma; neurons; extracellular matrix; hydrogels; mechanobiology; proliferation.

Contents

1 Introduction

1.1 Studying glioblastoma *In vitro*

Primary brain tumors (PBT) are a diverse group of abnormal and excessive tissue growths that are highly **aggressive** and difficult to **treat with therapies** [1]. Brain tumors can be classified into different histological classes based on the tumor tissue characteristics (e.g. origin, and molecular structure). The largest category is comprised of **neuroepithelial tumors**, which stem from central nervous system stem cells that later differentiate into **neurons** and **glial** cells. This class of tumors encompasses all types of **gliomas**, including **glioblastoma** and **astrocytoma**. Other important PBT subtypes comprise meningiomas, originating from meningothelial cells, and primary brain lymphoma, arising from B-lymphocytes and T-cell lymphocytes. **Gliomas** are the most common form of central nervous system (CNS) tumors originating from glial cells (e.g. astrocytes, oligodendrocytes, ependymal cells, and microglia), and among PBTs, **glioblastoma multiforme** (GBM) is the most aggressive.

1.1.1 GBM epidemiology

GBM is classified as a World Health Organization (WHO) **grade IV** brain tumor, characterized by a median survival of **12–15 months** from diagnosis. Only about **3–5%** of patients survive for 3 years or more [2], making GBM one of the most lethal human cancers [3]. It predominantly affects older adults, with a median age of diagnosis of 64 years [4]. Variations in incidence and mortality rates based on gender, race, and ethnicity can reveal underlying biological and environmental factors influencing GBM [4]. Specifically, men have a higher incidence of GBM compared to women, with an incidence rate being 1.6 times greater in males than in females [5].

Due to its highly **infiltrative nature**, **genetic heterogeneity**, and **protection by the blood-brain barrier (BBB)**, GBM is currently one of the **most challenging tumors** to treat and continues to carry an extremely poor clinical prognosis. **Complete tumor resection** is almost **impossible**, leading to high rates of recurrence and the presence of **intertumor** and **intratumor heterogeneity** together with changes in the BBB protection between blood vessels and brain tissue, complicate effective targeting with therapies.

- **Intertumor and intratumor heterogeneity**: Depending on the genetic mutations involved, **GBMs** can be categorized into four distinct subtypes: **mesenchymal**, **classical**, **proneural**, and **neural** [6].
  Each subtype is defined by specific **genetic mutations**. Mesenchymal GBMs often feature mutations in the **neurofibromin 1**(NF1), **PTEN**, and **TP53** tumor suppressor genes [6]. The classical subtype is marked by **EGFR** amplification but typically lacks TP53 mutations. **Proneural GBMs** are frequently associated with mutations in **TP53**, **IDH1**, and **PDGFRA** [6]. This **genetic diversity** contributes to significant **intertumor heterogeneity**, meaning that the same tumor can be present in various form depending on its genetic origins (Figure 1 a).

  At the **intratumor** level, considerable variability is also observed. Within a single tumor, different cell populations can exhibit varying behaviors, leading to **diverse responses to treatment** (Figure 1 b). This intratumor heterogeneity results in substantial variability in drug resistance among different cells of the same tumor, complicating the treatment process .

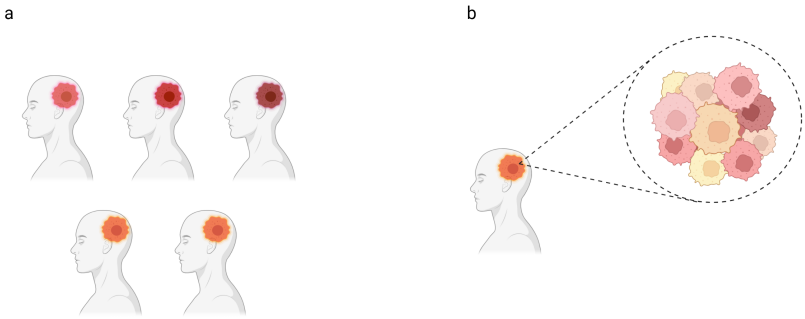

Figure 1: GBM tumor heterogeneity. a: Intertumor heterogeneity GBM may manifest differently in individual patients due to the activation of different oncogenic pathways specific to each patient. **b: Intratumor heterogeneity** cells within the same tumor from the same patient exhibit varying behaviors and responses to treatment.

- **Blood-brain barrier (BBB)**: The **BBB** is a protective layer composed of endothelial cells and it separates the circulatory system from the extracellular space of the CNS. The tight junctions between endothelial cells are less than 1 nm in size [6] and effectively **block more than 98% of small molecules** from passing through. In GBM tissues, the permeability of the BBB is increased, but the **increase is not uniform** throughout the tumor. This means that some regions of the tumor may have higher permeability than others and even when a drug manages to cross the barrier, the **upregulation of efflux pumps** by GBM cells membrane proteins can result in the chemotherapeutic agents being expelled before they can exert their effects.

1.1.2 GBM pathology

The precise origin of GBM has not yet been identified. Gaining a clearer understanding of it would be extremely beneficial to develop more effective therapies that target specific cellular pathways. The most widely accepted theory regarding cancer evolution and growth is the **hierarchical cancer stem cell (CSC)** model, which suggests that tumors originate from CSCs. CSCs arise from **mutations** in either normal **embryonic stem cells (ESCs)** or **progenitor cells**[7].

Stem cells are characterized by their abilities for **self-renewal**, **proliferation**, and **differentiation**. Among these, **ESCs** are the **most primitive** and are **pluripotent**, meaning they can differentiate into any cell type [7]. In addition to ESCs, there are other stem cells such as **neural stem cells** (NSCs), **mesenchymal** (MES) stem cells, **endothelial progenitor cells**, and **hematopoietic stem cells** (HSCs). These are categorized as **multipotent** stem cells, with a more restricted differentiation capacity compared to ESCs; for instance, neural stem cells can differentiate into neuron and glial progenitor cells [7]. According to the hierarchical CSC model, a tumor originates from **CSCs** that result from **genetic mutations** in normal **ESCs or progenitor cells**. These mutations may be present from birth or accumulate over time, leading to cells with the potential for uncontrolled growth[7].

During normal embryonic development and in the adult brain, normal NSCs in the cerebral subventricular zone of the brain, generate glial and neuronal cells. GBM stem cells may arise from NSCs and/or glial precursor cells by activating oncogenic pathways [8]. In GBM progression, many genetic alterations play a crucial role in activating different signaling pathways that result in huge changes in cellular metabolism and proliferation.
Many mutations are linked to the **TP53** gene and the **phosphatase and tensin homolog (PTEN)** gene (tumor-suppressor genes), **the epidermal growth factor receptor (EGFR)** (regulator in cell proliferation, differentiation, division, survival, and cancer development), and the

platelet-derived growth factor receptor (PDGFR) which regulates cell proliferation, cellular differentiation, cell growth, development and many diseases including cancer.

The receptor activation leads to different signaling pathway stimulations (e.g. tyrosine kinase receptors pathways), therefore, changes and overexpression of receptor activity dramatically affect cancer growth[9].

- **TP53 - PTEN mutations**: TP53 encodes the p53 protein that plays a central role in maintaining cellular homeostasis (e.g. ion concentration and pH balance in the cellular microenvironment) and is usually deregulated in cancer [10].
  p53 prevents the cell cycle from progressing in case of DNA damage, genotoxicity, oncogene activation, aberrant growth signals, and hypoxia [10].
  TP53 mutation is linked to **p53-ARF-MDM2/4** pathway activation. Indeed, MDM2 and MDM4 proteins enhance the incorrect regulatory activity of p53 protein leading to the loss of various tumor suppressor functions which results in tumor proliferation [10]. PTEN protein as well, controls cell growth, proliferation, and survival. It acts as a **phosphatase** regulating the PI3K/Akt pathway through hydrolysis reactions, which affects cellular growth, proliferation, and metabolism. Mutations or deletions in PTEN that impair its phosphatase activity can lead to uncontrolled cell growth and contribute to the development of cancer [11].
  PTEN is an enzyme with both lipid and protein phosphatase activities. It dephosphorylates the lipid phosphatidylinositol 3,4,5-trisphosphate (PIP3), converting it into phosphatidylinositol 4,5-bisphosphate (PIP2). Conversely, phosphatidylinositol 3-kinase (PI3K) phosphorylates PIP2 to regenerate PIP3. This interplay between PTEN and PI3K maintains a balance that prevents uncontrolled cell growth and division. Mutations in the PTEN gene disrupt this balance, leading to unchecked cell proliferation (Figure 2).
- **EGFR - PDGFR mutations**: **EGFRs** and **PDGFR** belong to the family of receptor **tyrosine kinases (RTKs)**, which act as receptors for growth factors. These receptors are situated on the cell surface. They are activated by specific molecules (ligands), which trigger various signaling pathways like **Ras/MAPK/ERK and Ras/PI3K/AKT** which are crucial for processes such as cell growth, differentiation, and the formation of new blood vessels (angiogenesis). EGFRs are associated with cell proliferation and play a role in the development of glioblastoma and resistance to treatment. On the other hand, **PDGFR** signaling is important for the normal development of tissues, and when disrupted, it contributes to the development of cancer (Figure 2).

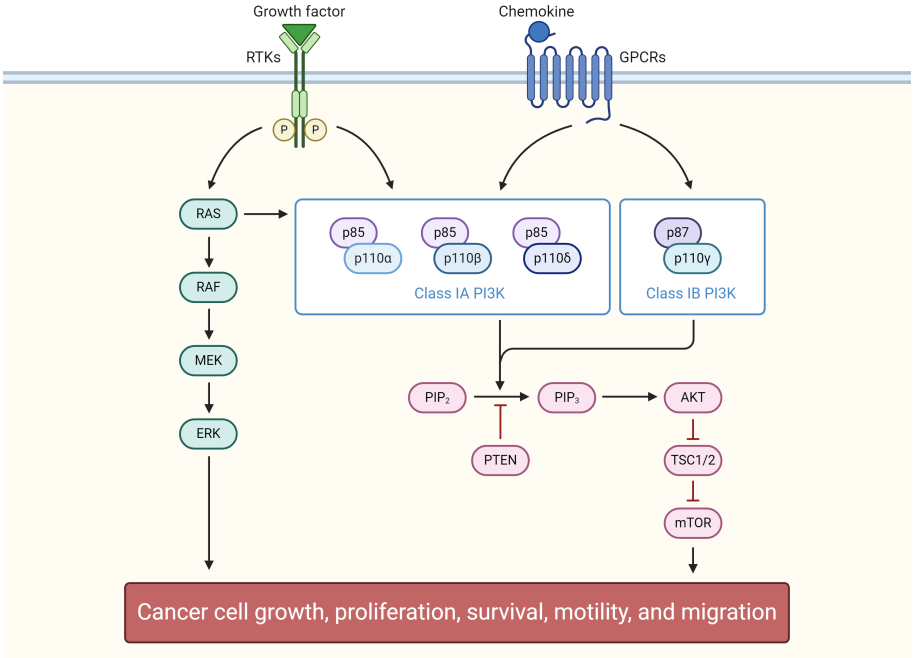

Figure 2: PI3K pathway in GBM. PI3K pathway is activated by surface receptors from the RTs family. When PI3K is activated by upstream signals, PIP3 is generated from PIP2 and activates downstream signaling pathways, such as the AKT/mTOR which affects cell growth, proliferation, survival, motility, and migration. PTEN is responsible for converting PIP3 to PIP2, helping to maintain cellular balance.
© BioRender.com

1.2 *In vivo* models

So far, *in vivo* transplants of GBM in animal models have been used to study tumor development upon the engraftment of human cells and tissues into nude mice[12].
Nude mice have a genetic mutation that prevents the development of a functional thymus, resulting in **immunodeficient organisms**, making them ideal for studying cancer **without rejection of the tumor** after injection and for conducting studies on drug response. The key disadvantage, however, is that these tumor models are grown on an **immunodeficient** background, which does not allow for characterization of the GBM immune landscape or evaluation of **immunotherapies** [13].

Patient-derived tumor cells and tissues are typically implanted into the subcutaneous flank location of nude mice to facilitate tumor visualization and manipulation [12]. However, due to the non-natural location, analysis of tumor diffusion, progression, and response to drugs is **significantly limited** [12].
For this reason, **orthotopic** implantation of GBM in the brain is more extensively used, as it provides a better understanding of the human brain extracellular matrix and the tumor microenvironment. Patient-derived xenografts are efficient as they preserve **tumor heterogeneity** and **histological characteristics**, allowing for personalized drug efficiency tests in individual patients[14]. However, there are limitations, including the fact that immunodeficient rodents **may not respond to certain drugs**, and the surrounding **microenvironment of mouse origin** may interfere with drug response.

Another approach in *in vivo* cancer studies is to use **genetically engineered mice**. Cancer arises and progresses mostly due to genetic mutations that alter various cell signaling pathways, ultimately leading to **uncontrolled cell proliferation** without cancer suppression. For these

purposes, mice have been genetically engineered to express specific genes involved in tumor formation. **Viral vectors** are used to introduce specific genetic material into cells, including genes that are perfectly integrated into the mice genome and then drive tumor development[15].
Among the different mutations that can be induced, some of the most important are the mutations in the **p53** tumor suppressor gene, the introduction of **EGFRvIII** (a mutant form of EGFR), or the loss of **PTEN protein**, which activates the Ras/MAPK/ERK and Ras/PI3K/AKT pathways[14] as described in section 1.1.2.

Given the limitations of animal models in replicating the specific environment of GBM cells in the human brain, it is crucial to advance the development of *in vitro* 2D and 3D models.
In vitro models are particularly valuable because they provide **precise control over experimental conditions** and **reproducibility**, advantages that are challenging to achieve *in vivo* due to the inherent biological variability of living organisms.
They can be designed to closely mimic the composition of both healthy and cancerous tissues facilitating the simulation of diverse conditions and replicating the heterogeneity of the human brain tissue, which is essential for understanding disease progression and drug responses.

1.3 2D and 3D *in vitro* models

At the current state of the art, the examination of GBM interactions within the brain environment has been significantly propelled by advances in *in vitro* models [16]. There are various *in vitro* models of the GBM microenvironment, including 2D and 3D models, organoid and spheroid cultures.

- **2D models**: cells are placed on **rigid plastic** or a **monolayer of ECM mixture** and kept in a cell medium supplemented with ECM proteins such as **collagen** and **laminin** [13] (Figure 3 a). However, it is essential to consider that 2D models **oversimplify** the extracellular environment and **alter** as well cells' **growth, morphology, phenotype, biochemical properties, functionality, signaling, and drug response**[17][18]. In 2D models, cells grow on flat surfaces, allowing a higher portion of the cell to be directly in contact with the medium, facilitating access to nutrients and oxygen. This aspect is subject to **greater variability** in real tissues due to the 3D cellular network architecture[18].
- **3D models**: to study cancer in 3D, multicellular tumor spheroids (MCTS) are used.
  Spheroids are clusters of cells seeded either in suspension or embedded in gel scaffolds. This approach provides a more accurate model of cancer growth by reflecting various aspects of tumor biology, including **cell differentiation, migration, and the diverse phenotypes and morphologies** influenced by the mechanical and chemical properties of the surrounding matrix. MCTs models also better replicate the oxygen and nutrient gradients that cells experience within the extracellular matrix, offering a more realistic insight into drug resistance.

In 3D culture systems, spheroids can be grown in suspension, within microfluidic devices, or in hydrogel matrices.

1. **Suspension cultures**: The main features of this method are a serum-free, an artificially low adhesion cell growth microenvironment, and a high concentration of growth factors in the culture medium[19]. In this model, most tumor cells grow and aggregate into a spheroid form with a diameter ranging from 20 μm-1 mm [19] and then float in the cell medium without adhering to the culture plate (Figure 3 b).

2. **Device-assisted culture**: magnetic levitation method, spinner bioreactor culture, and microfluidic devices are all improvements of the suspension culture.
   In **magnetic levitation**, cells are treated overnight with magnetic nanoparticles in solution that bind to them. When a magnetic field is applied above the dish, the cells are kept suspended in the medium, preventing them from adhering to the dish surface. This approach eliminates the need for coatings and facilitates the formation of 3D cell clusters as the cells aggregate together (Figure 3 c).

   The **spinner bioreactor** system includes a container to hold the cells culture and a paddle stirring continuously to keep the cells suspended, medium well mixed and to obtain uniform cellular spheres [19]. This setup has been used to develop various tumor models, including hepatocellular carcinoma, neuroblastoma, breast adenocarcinoma, and melanoma [19] (Figure 3 d).

   To have better control over the spheroid's size and the cell medium conditions, instead, a **microchannels structure** with dimensions of 1–1,000 μm has been developed [19]. In these platforms, fluid continuously flows through microchannels, simulating the effects of *in vivo* vascularization. This, combined with precise control over micro-liquid quantities, contributes to the faster formation of spheroids (Figure 3 e).

3. **Gel embedding culture** : while 3D suspensions are useful for studying drug resistance in cancer cells, they do not fully capture **the complexity of the ECM** and its **interactions with cells**. On the other hand, hydrogels with embedded spheroids offer a more detailed model by not only supporting 3D cell cluster formation but also incorporating the complex structure of the extracellular matrix (Figure 3 f).
   This approach more accurately represents both **cell-cell** and **cell-ECM** interactions.[20] Various polymer combinations can be utilized to replicate the chemical compositions and mechanical properties of the brain extracellular matrix, such as collagen, gelatin, alginate, and matrigel. Additionally, synthetic polymers can be used for their **superior stability** in terms of **temperature** and **mechanical degradation**[21].

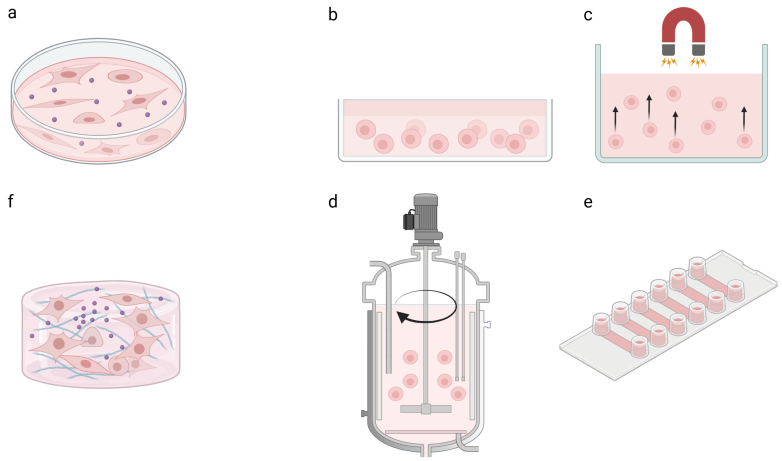

Figure 3: 2D and 3D *in vitro* models for GBM culture. a: 2D culture of cancer cells, **b, c, d, e:** 3D culture of GBM cells in spheroid form, utilizing techniques such as suspension culture, magnetic levitation, spinner bioreactors, and microfluidic devices, **f:** 3D culture for GBM cells embedded in hydrogel scaffolds.

1.4 Hydrogels

Hydrogels are **crosslinked polymer chains** with **3D network** structures that can absorb **large amounts of liquid** in their **porous** structure [22]. Therefore, thanks to their high water content and porosity, they can resemble **living tissues**. Hydrogels can be classified in many different ways, depending on the **polymer composition**, the **crosslinking method**, their **electric charge**, and their **stimuli response**. [23].

1.4.1 Hydrogel chemical composition

- **Natural polymers**: **polysaccharides**(e.g. cellulose, alginate, carrageenan), **polyamides** (e.g. collagen), **biological polymers** (e.g. nucleic acid and DNA), **polyphenols** (e.g. lignin), **organic polyesters**, **inorganic polyesters** (e.g. polyphosphazene), and **polyanhydrides** (e.g. poly sebacic acid) [24]. Being of natural origin, natural polymer-based hydrogels are highly similar to the extracellular matrix, resulting in **high biocompatibility**.
- **Synthetic polymers**: are produced through chemical reactions. Monomer molecules of the same type are forced to react together by an **initiator molecule**. The initiator, triggered by the temperature, light, or pH, indeed, creates a reactive center in the monomer (e.g. by breaking a double bond) that starts a **chain reaction** and, leads, in the end, to the formation of the polymeric chain.
- **Hybrid polymers**: are a combination of the previously mentioned polymers. **Natural biopolymers** such as gelatin, chitosan, and dextran have been combined with **synthetic polymers**. This results in the **substitution of some functional groups** of the natural polymer, allowing the engineered polymer to be capable of photocrosslinking. These polymers show great promise for constructing *in vitro* matrices as they maintain good biocompatibility while also being more stable both mechanically and chemically.

1.4.2 Hydrogel crosslinking processes

- **Physical crosslinking**: is the formation of a bond between polymer chains through **molecular entanglement** or **weak physical interactions** such as **ionic interactions, coordination bonding, hydrogen bonding, and van der Waals interactions**.

  1. **Ionic interactions**: polyelectrolyte polymers can undergo **ionic crosslinking** because of their ionic groups, which dissociate in water-based solutions to release **ionic charges**. This dissociation allows the polymers to interact with charged species through electrostatic interactions [25].
     An example of this process is **sodium alginate**, which contains carboxyl groups with a negative charge neutralized by sodium ions with a positive charge. In the presence of calcium ions, which carry a double positive charge (e.g. dissociated ions from a calcium chloride solution), sodium ions are replaced by calcium ions. This replacement forms ionic crosslinks between different alginate polymer chains by bridging the carboxyl groups (Figure 4 a.1).
  2. **Coordination bonding**: this kind of bonding occurs when a molecule or an atom donates a pair of electrons to another atom. It differs from the usual covalent bond because, in this case, electrons **are not shared** between the two atoms. Therefore, in the case of physically crosslinked gels, functional groups such as carboxylate or phosphonate groups present in the polymeric chains, **act as ligands**, coordinating with **transition metal ions**.
  3. **Hydrogen bonding**: directional bonding where a **hydrogen atom** is attracted to an **electronegative atom**, such as oxygen, nitrogen, or fluorine, in a different molecule.

In this case, therefore, hydrogen atoms are crucial to bind together polymeric chains [26] (Figure 4 a.2).

4. **Change in temperature**: For natural polymers such as k-carrageenan, agarose, or gelatin, a change in temperature is often enough to induce crosslinking of the polymer chains. Typically, these polymers, initially in powder form, are dissolved at high temperatures, around 80°C. After dissolving, the solution is cast into a mold, and a **rapid decrease in temperature** causes the polymer chains to **physically crosslink**, forming a gel structure.

These interactions rely on external changes in pH, ionic strength, and temperature. Therefore, this crosslinking process has limited durability and low mechanical and thermal stability.

- **Chemical crosslinking**: The hydrogel consists of covalently cross-linked networks, where polymer chains are interconnected through **covalent bonds**. This cross-linking process limits the rotational freedom of the polymer chains, leading to a hydrogel with **increased rigidity, mechanical strength, chemical stability, and brittleness** [27].

  Functional group reactions: Some crosslinkers have two or more reactive sites that can covalently bond with different functional groups, linking various polymer chains together. This cross-linking process forms a three-dimensional polymer network, enhancing the **structural integrity** of the material. The interconnected covalent bonds provide the hydrogel with increased **mechanical strength**, **improved chemical resistance**, and enhanced **dimensional stability** (Figure 4 b.1).

  Free radical polymerization: In the presence of an **initiator molecule**, exposure to external stimuli such as **visible or UV light**, **temperature changes**, or **pH variations** generates highly reactive species known as **free radicals**. These radicals are essential for initiating the polymerization process. Upon activation, the initiator **decomposes** into **two free radicals**, which react with the polymeric chains, creating new free radicals (e.g. breaking a carbon-carbon double bond). When radicals from different polymer chains interact, they form **covalent bonds** that link the chains together [28] (Figure 4 b.2).

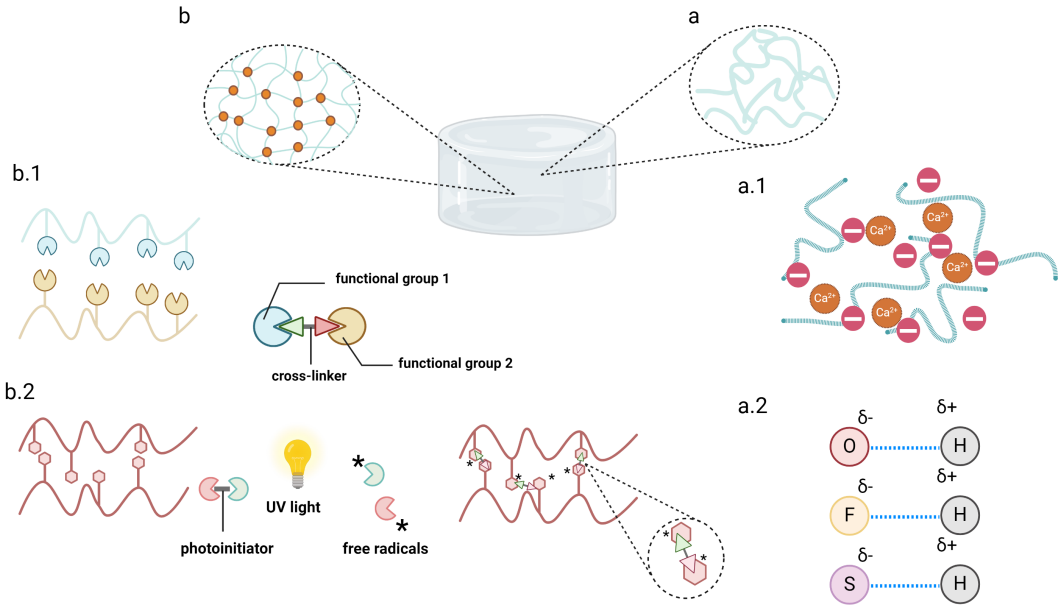

Figure 4: Hydrogels crosslinking methods. a: Physical crosslinking, b: Chemical crosslinking. a.1 Ionic bonding: in the presence of ions, charged polymeric chains form crosslinks through electrostatic interactions, **a.2 Hydrogen bonding:** hydrogen atom is attracted to an electronegative atom, such as oxygen, sulfur, or fluorine, **b.1 Functional groups reaction:** the crosslinker binds to the two polymer chains end to make it crosslink, **b.2 Free radical polymerization under the UV light exposure:** the photoinitiator undergoes a process in which it splits into two free radicals. These radicals then propagate the formation of radicals along the endings of the polymer chains, rendering them reactive and capable of crosslinking.

.

1.5 Hydrogels to mimic the brain and GBM extra-cellular matrix

The natural extra-cellular matrix is a structural support network made up of different polysaccharides, proteoglycans, proteins, receptors, and growing factors that promote cell proliferation and many different signaling pathways.

1.5.1 Brain extracellular matrix composition

- **Polysaccharides**: **glycosaminoglycans** (e.g. keratin sulfate, heparin sulfate, dermatan sulfate, and hyaluronic acid) are **negatively charged** (due to sulfate and carboxyl groups) unbranched polysaccharides that are usually covalently attached to proteins, forming **glycan-protein conjugates**. Among them, Hyaluronic Acid is the most important one, especially when it comes to GBM cancer due to the key role it plays in GBM cells' metabolism, morphology, and phenotype modification.
- **Proteoglycans**: **glycoprotein**in which the protein core is a central polypeptide chain that provides a scaffold for GAGs (e.g. hyaluronan, fibrous matrix proteins, such as collagen) covalent attachment [29]. They are involved in binding cations such as sodium, potassium, and calcium, as well as water, but growth factors and matrix proteins [30].

- **Diverse proteins**: **fibrous proteins** (glycoproteins) such as collagen, elastin (structural proteins), laminins (adhesion proteins), which provides **mechanical support** to cells and also dramatically affects cells proliferation, differentiation, morphology and migration regulating cell-matrix interactions.

  Collagen is a crucial fibrous protein in the extracellular matrix of human organs, known for its significant mechanical support due to covalent intramolecular and intermolecular bonds between its polymeric chains [31].
  Elastin, another essential fibrous protein in the brain's ECM, is composed of about 33% glycine, 10–13% proline, and over 40% other hydrophobic amino acids [32]. This composition not only contributes to elastin's exceptional stability but also allows it to return to its original shape after being stretched[32].
  In contrast, **laminins** are the primary **cell-adhesive** proteins found in the basement membrane [32]. They are organized into various layers, where different types of laminins are combined. These laminins bind to cell surface receptors such as heparin, integrins, and α-dystroglycan, promoting cell adhesion to the extracellular matrix [32].

- **Receptors**: among the different receptors, **integrin** is crucial in the cell's mechanical stability as it links the cell's cytoskeleton with the basement membrane [32]. It also plays a crucial role in terms of **intracellular signal transduction** contributing to changes in the electrical activity of a cell.

- **Growth factors**: they affect cell behavior by promoting cell adhesion, growth, proliferation, and differentiation during nervous system development [33]. Among all the growth factors, the most important are the **epidermal growth factor (EGF)**, which initiates mitosis and promotes rapid cell growth, the **vascular endothelial growth factor (VEGF)**, which controls brain angiogenesis and vascular network formation within the brain ECM. **Fibroblast growth factors (FGF)** regulate embryonic development, organogenesis, and tissue differentiation. **Brain-derived growth factor (BDNF)** serve as a survival factor during early ECM development.

1.5.2 Brain and tumor extracellular matrix mechanical properties

The brain is a **mechanosensitive organ**, thus changes in the mechanical properties of the extracellular matrix have a high impact on many physiological and pathological processes [34]. Rheological measurements reveal that brain tissue is a **viscoelastic material**. At **low-stress** levels, it behaves like a **solid**, quickly returning to its original shape. In contrast, at **higher stress** levels, it undergoes **plastic deformation** and acts more like a **liquid**, losing its original shape[35].
Mechanical forces exerted by the ECM affect healthy neuronal network activity, axonal extension, neuron-astrocyte communications, as well as neuron-ECM interactions and disease progression [34]. Compared to other organs, the ECM of the brain is distinct due to its predominance of **non-fibrous components**, which contribute to the brain's **relatively soft tissue texture** (Young's modulus between 0.1kPa for the young brain and 1kPa for the adult brain) [36]. In this case, the ECM plays a crucial role in both the development of a healthy adult brain and in the progression of brain diseases [37].

Moving to cancer tissue, even though genetic modifications initiate cancer, then it develops by altering its physical environment through **mechanotransduction** [29]. In the tumor microenvironment, increased secretion and remodeling of fibrous ECM proteins, such as laminin, collagen, or fibronectin, lead to a huge increase in tissue stiffness (up to 26 kPa) [38]. Stiffening of the brain ECM due to the overexpression of brain fibrous proteins and receptors exposes GBM cells to a high mechanical stress that makes them reshape, proliferate, and change phenotype.
In response to the increase in the ECM stiffness, cancer cells activate **responsive signal pathways** to **reinforce** the cell's cytoskeleton which then leads to an increase in cells' adhesion and proliferation [39].

In addition to the fact that cancer cells contribute to the remodeling and alteration of the mechanical properties of the extracellular matrix and in response to these changes, the cells themselves enhance the rigidity of their cytoskeleton. Among all the factors that undergo overexpression during the tumor progression, **hyaluronic acid** plays a key role. The brain ECM is composed of 25% HA in mass, which gradually increases during GBM tumor progression (Figure 5) [38].

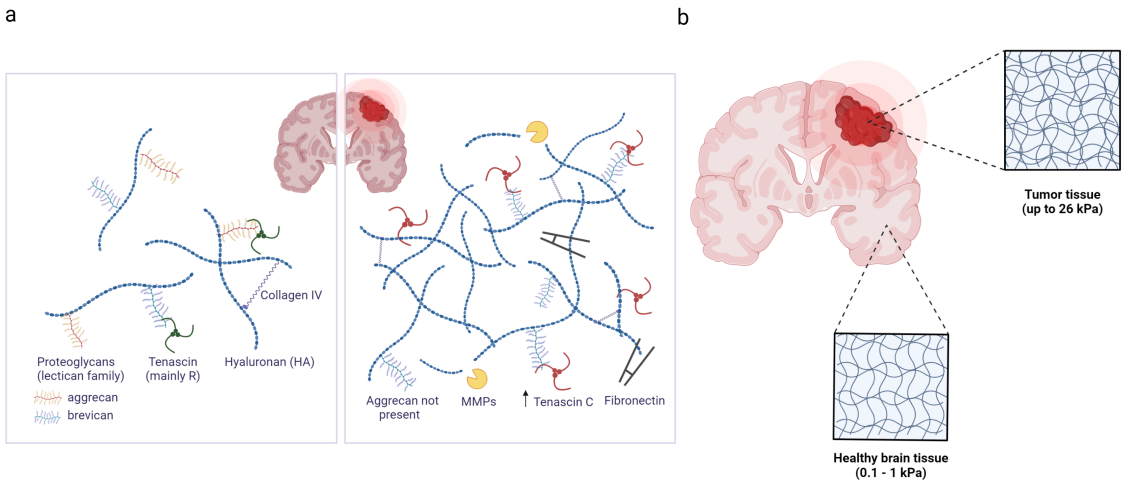

Figure 5: Brain and tumor extracellular matrix. a Composition of the brain and GBM tissue: the provided figure illustrates the differences in mechanical properties between healthy and diseased brain tissue. Brain tissue comprises proteoglycans (aggrecan, brevican), hyaluronic acid, tenascins (specifically tenascin R), and collagen IV. In contrast, glioblastoma ECM demonstrates increased stiffness and contains neurodevelopmental proteins (tenascin C) and metalloproteases (MMPs) that promote invasion, **b: Hydrogels to mimic healthy and brain tissues:** the concept involves replicating the tumor and brain matrices using a less stiff gel to mimic healthy tissue and a stiffer gel to represent tumor tissue.

1.5.3 Haluronic acid's role in GBM tumor spreading

HA is a **linear polysaccharide** consisting of a repeating unit of disaccharide: D-glucuronic acid and N-acetyl-D-glucosamine [40]. In the brain extracellular matrix, HA is one of the most versatile molecules thanks to the fact that each monomer presents **three different types of functional groups** (—hydroxyl, carboxyl, and amide) through which it can attach many different molecules (e.g. the carboxylic acid and primary alcohol are important for both recognition by hyaladherins and for chemical modification, the amide also supports adhesion)[41].
Cells bind to HA polymeric chains through the cell's surface receptors (e.g. CD44 and RHAMM), and in this way, HA concentration in the extracellular matrix can **activate precise signaling pathways** in the cell that results in the modification of cell cytoskeleton, shape, and morphology[41].
Extracellular mechanical properties (e.g. Young's modulus and crosslinking degree), affect the binding degree of the cell's surface receptors such as CD44 with HA, thus CD44 can undergo **force-dependent switching** between low affinity and high affinity HA-binding states [41]. Cell's metabolism and signaling pathways are influenced by the stiffness of the extracellular matrix, and as a result, the cell's response to the mechanical properties of its environment leads to the production and secretion of hyaluronan synthases and degradation by hyaluronidases, which in turn increases the stiffness of the extracellular matrix in a closed loop cycle [41].

1.5.4 Synthetic hydrogels to mimic the ECM

Hybrid hydrogels offer an ideal solution for recreating both healthy and cancerous extracellular matrices *in vitro*. They maintain excellent biocompatibility while allowing for precise control over mechanical properties across a broad range of stiffness. This is achieved by incorporating specific functional groups into the natural polymers, which enables chemical crosslinking and enhances both mechanical and chemical stability .

- **Hyluronic acid**: as described in 1.5.3, hyaluronic acid (HA) consists of repeating disaccharide units and features numerous functional groups that enable various chemical modifications. These reactive functional groups facilitate cross-linking between polymer chains. A widely used method for modifying HA involves introducing **thiol** functional groups to enable covalent cross-linking between different polymer chains [42]. Thiol groups (-SH) are characterized by a sulfur atom bonded to a hydrogen atom. When two thiol groups from separate polymer chains come into proximity, they can form a **disulfide bond (-S-S-)** through an oxidation reaction due to their high reactivity.
  In addition to thiol modifications, HA can also be altered through its hydroxyl, N-acetyl, and carboxylic groups [43]. The main chemical modification techniques for hyaluronic acid (HA) involve esterification, etherification, amidation, and oxidation of the functional groups at the ends of the polymer chain. A widely used method is reacting HA with **methacrylic anhydride**, which facilitates the etherification of hydroxyl groups in basic solutions. This modification enables the polymer to be easily cross-linked under **UV light** in the presence of a crosslinker [43].
  The interest in this polymer stems from its ability to enhance the understanding and replication of the human brain when combined with other naturally derived polymers such as collagen or gelatin.
  Recent studies have focused on collagen-based hydrogels incorporating HA [21]. Collagen-based hydrogels initially exhibit an elastic modulus of approximately 300.48 ± 39.5 Pa [21], which can increase to over 1000 Pa with the addition of HA. This finding is significant as it highlights the potential of hyaluronic acid to **adjust the mechanical properties** of hydrogels, achieving stiffness levels that more **closely match** the average stiffness of **cancer tissue**.

- **Gelatin Methacryloyl**: this synthetic polymer is derived from the chemical modification of gelatin, a natural hydrophilic polymer produced through the hydrolysis and denaturation of collagen at high temperatures [44]. Gelatin is particularly suited for creating 3D matrices that mimic the brain ECM due to its inclusion of the Arg-Gly-Asp (RGD) sequence, a polypeptide sequence that interacts with cell surface receptors such as integrins, thereby promoting cell attachment and adhesion. However, gelatin is **highly thermally unstable**, necessitating chemical modifications to enable crosslinking .
  Gelatin's side chains contain numerous reactive groups, including -OH, -COOH, -NH2, which make it relatively straightforward to chemically modify [44]. The polymer is synthesized by reacting gelatin with methacrylic anhydride, replacing the amino and hydroxyl groups in the gelatin polymer chains with methacrylate groups that are highly reactive to UV light. The presence of a crosslinker allows for the formation of covalent bonds between polymer chains, resulting in a more stable mechanical structure.
  Common free radical photoinitiators used for this process include 2-hydroxy-4-(2-hydroxyethoxy)-2-methylpropiophenone (IC-2959) and lithium phenyl-2,4,6-trimethylbenzoyl phosphinate (LAP) [45]. LAP absorbs UV light with a wavelength of 405 nm, producing two highly reactive free radicals. These radicals efficiently break the vinyl bonds between the carbon atoms of the methacrylamide and hydroxymethacrylate groups, creating a stable three-dimensional network.

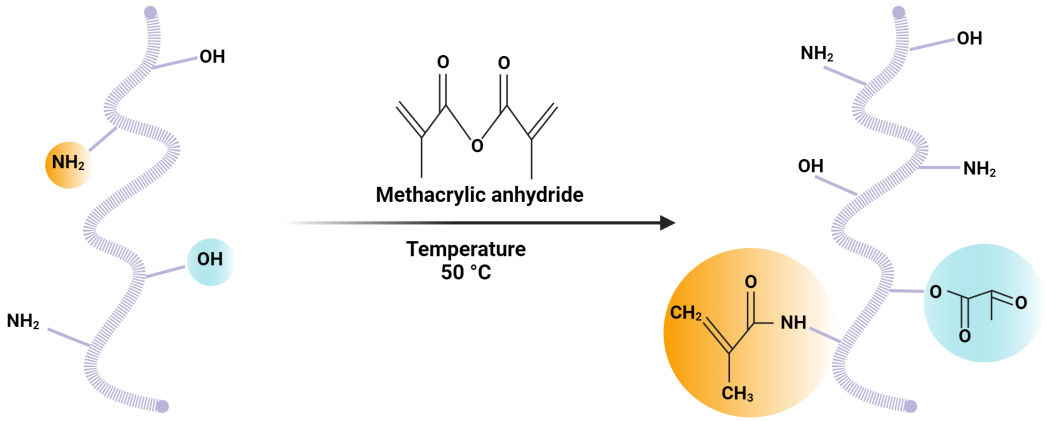

Figure 6: Gelating substitutional process. The figure illustrates the substitution process of amino and hydroxyl groups in the gelatin polymer with methacrylate groups, which are highly reactive to UV light. This makes gelatin chemically cross-linkable, enhancing its mechanical properties.

1.6 Motivation and Aim

This thesis explores the advantages of using hydrogels to study neural tissues affected by glioblastoma. The study begins by replicating the mechanical properties of both healthy neural tissues and GBM tumor microenvironment. While the mechanical properties of healthy tissues are well-documented, information on the mechanical characteristics of GBM is limited.
To address this, the research involves collecting global and local measurements from surgically resected GBM tumors. Subsequently, GelMA hydrogels are engineered to match the mechanical properties of each tumor microenvironment. Human induced pluripotent stem cell-derived neurons and primary glioma cells are then cultured in these hydrogels to access cell growth, phenotype, migration, and interaction.

Goals

1. How does the concentration of polymers and their chemical composition affect the mechanical properties of hydrogels?
2. How do hydrogel stiffness and chemical composition impact cancer cell growth, proliferation, phenotype, migration, and interactions?
3. How do hydrogel stiffness and chemical composition impact neurite elongation and branching?
4. How can we optimize the coculture of neurons and glioblastoma by creating a multi-hydrogel platform using PDMS microstructures?

Addressing these questions is essential for designing robust 3D hydrogel scaffolds that more accurately replicate the extracellular matrix. This improved model of the human brain's complex behavior *in vitro* will enable more effective targeting of tumors with therapies.

2 Materials and Methods

2.1 Materials

Component	Catalog Info
Antibiotic Antimycotic 1X	Sigma, A5955-100 ml
BDNF	PeproTech, 450-02
B27 Plus supplement 50X	Thermo Fisher, A3582801
B27 without Vitamin A 50X	Gibco, Thermo Fisher Scientific 12587-010
CNG Medium Stock	n.a.
Chk mAb to GFAP	abcam, AB4674
DMEM/F12 1:1	Sigma, D8062
Doxycycline	Fisher Scientific, NC0424034
EGF (500 μl/ml)	
FGF (250 μl/ml)	
Gelatin Methacryloyl	
Glutamax	Thermo Fisher, 35050-061
GDNF	PeproTech, 450-10
Glutagro/Max 1X	
Goat anti-chicken Alexa Fluor 647	Thermo Fisher Scientific 2480082
Goat anti-Mouse Alexa Fluor 555	Thermo Fisher Scientific 2552975
Goat anti-Rabbit Alexa Fluor 488	Thermo Fisher Scientific 2521157
Goat Serum	Sigma Aldrich
Heparin 1000X	Stemcell, CAT#07980
Hyaluronic Acid Methacrylate Hoechst 33342	Termo Fisher Scientific 2528096
LAP (1X)	
Laminin	Sigma Aldrich, L2020-1MG
Methacrylic anhydride	
Ms mAb to Nestin (0.5 mg/ml)	abcam, AB6320
N2 supplement 100X	ThermoFisher, 17502-048
Neurobasal Plus Media	ThermoFisher, 21103-049
Neurosphere Medium Stock (Primary Tumor)	n.a
NGN2 iNeurons	Novartis hDFa90/1.2iNgn2 p8+35
Non-Essential Amino Acids 1X	
Paraformaldehyde	Sigma Aldrich, 1004960700
PBS (1x)	Gibco, Thermo Fisher Scientific 10010015
Polydopamine	Sigma Aldrich
Polyvinylpyrrolidone	Sigma Aldrich
Primary Glioma cells	
Rb mAb to Ki67 (0.031 mg/ml)	abcam, AB16667
Rho-kinase inhibitor	Sigma Aldrich Y27632, 688000
Sodium Bicarbonate 1X	
Sodium Pyruvate 1X	
TRIS (10mg/ml, pH 8.5)	
Triton X-100	Sigma Aldrich

Table 1: List of media components, primary and secondary antibodies, gel components, and cell lines utilized in the experiments.

Component	Catalog Info
Centrifuge	Eppendorf, 5810 R
CLSM	Olympus, Fluoview 3000
Ibidi glass dishes	Ibidi
Ibidi 18 well plates	Ibidi
Fluid Force Microscopy	FlexAFM scan head (Nanosurf) and a C3000 controller driven by its original software (Nanosurf C3000 v. 3.3835), and a digital pressure controller unit (ranging from 800 to +1000 mbar) operated by a digital controller software (Cytosurge CORA)
Rehometer	Anton Paar mcr 302e

Table 2: List of instruments and materials used for experiments, including equipment for imaging and mechanical characterization, as well as components for storing the gels.

2.2 Methods

2.2.1 Hydrogel making

GelMA hydrogels

Different formulations of GelMA and HAMA have been utilized to create hydrogels with varying stiffness levels for the polymeric matrix. Initially, hydrogels made **exclusively of GelMA** were developed, with polymer concentrations ranging from approximately 3 wt% to around 10 wt% GelMA. The intention was to replicate conditions conducive to both neuronal and cancer cell growth. Adjusting the polymer concentration affected **polymer chains' entanglement**, altering the **network's mesh size**, **porosity**, and **density of attachment points**, which, in turn, influenced cell growth on the scaffold.

GelMA synthesis:

As outlined in section 1.5.4, GelMA is a synthetic polymer produced by chemically modifying gelatin with methacrylamide or hydroxymethacrylate groups. This process involves reacting gelatin with **methacrylic anhydride**, leading to the introduction of **methacrylate** side groups to the lysine and hydroxyl residues in gelatin. The synthesis of GelMA is a two-step process [44]. First, gelatin is dissolved in phosphate-buffered saline (PBS) (pH 7.5) at 50 °C, and methacrylic anhydride is then added to the solution. After an hour of reaction, the mixture is diluted fivefold to stop the reaction. Subsequently, the mixture is **dialyzed** against distilled water at 40 °C for 5 to 7 days to remove any unreacted methacrylic anhydride and is then lyophilized to obtain GelMA powder, which is stored at -20 °C.

GelMA stock solution

To prepare the GelMA stock solution, the polymer was dissolved in PBS at 37°C for approximately one hour. The quantity of polymer used depends on the desired final concentration of the gels. When working with very soft polymers at concentrations ranging from 2% to 5% wt, a 6.5% wt GelMA stock solution was utilized. For higher concentrations, specifically between 7% and 10% wt, a 13% wt GelMA stock solution was employed. To prepare the solution, 15 mg of GelMA powder was added to a 5 mL Eppendorf tube. The PBS volume was adjusted according to the final concentration needed. For example, to prepare a 10% wt stock solution, 150 μL of PBS was added. It is crucial to **fully dissolve** the polymer and avoid any residual undissolved powder. This is achieved by heating the solution on a heat plate to a maximum temperature of 42°C, which helps to dissolve the polymer **without compromising** the gelatin's **protein structure**. Once

completely dissolved, the stock solution was stored at -4°C.

GelMA hydrogels making

To prepare the gel, first, the stock solution was warmed in a dry bath at 37°C. Then, in a 50μl Eppendorf tube were added 2.75μl of laminin, 10 μl LAP, and then the correspondent amount of cell media and polymer. The content was then mixed with a 20μl pipette to ensure the correct distribution of all the chemicals. Given LAP's **sensitivity to UV light** and **oxygen**, it is essential to keep the UV light turned off under the hood when handling this cross-linker.
The hydrogel mixture was then poured into an 18-well plate, each receiving 15 to 20 μl of the mixture. The gels were cross-linked under UV light for 5 minutes. After cross-linking, each well was filled with either neuron media or cancer media, depending on the cell type to be seeded on the scaffolds, to prevent the gel from **drying out**. The concentrations of laminin and cross-linker were computed for a final volume of 50 μl for the hydrogel mixture. These volumes **remained constant**, with only the polymer and media concentrations being varied to reach the desired final GelMA concentration.

Hyaluronic acid and GelMA hydrogels

In our study, GelMA was combined with methacrylate-modified hyaluronic acid (HAMA) to investigate the complexity of the **human brain composition** in greater detail, focusing on the HAMA 0.8 wt% + GelMA 4.5 wt% formulation.

HAMA Stock Solution

The HAMA stock solution was prepared by dissolving the polymer PBS at 42°C for up to three hours due to its **higher viscosity** compared to GelMA. The quantity of polymer used depended on the desired final concentration of the gels. We initially attempted to test different concentrations of HAMA by preparing 2 wt% and 5 wt% stock solutions. However, the 5 wt% solution resulted too viscous, making accurate measurement with a 20 μl tip challenging. As a result, we used the 2 wt% stock solution and adjusted the gel formulation accordingly. Our goal was to modify the gel formulation by incorporating 1 wt% HAMA, with the rest as GelMA. To dissolve the powder, 15 mg of HAMA powder was added to a 5 ml Eppendorf tube. The PBS volume was adjusted according to the required final concentration (e.g., 750 μl of PBS was added to prepare a 2 wt% stock solution). It was essential to ensure complete dissolution of the polymer and avoid any residual undissolved powder. This was accomplished by heating the solution on a heat plate to a maximum temperature of 42°C, which facilitated dissolution without compromising the polymer's structure. Once fully dissolved, the final hydrogel mixture was prepared.

Hyaluronic Acid and GelMA Hydrogel Preparation

To prepare the gel, the stock solution was warmed in a dry bath at 37°C or on a heat plate at 42°C if the stock was particularly viscous. In a 50 μl Eppendorf tube, 2.75 μl of laminin and 10 μl of LAP were added, followed by the appropriate amounts of the two polymers (20 μl HAMA + 17.3 μl GelMa). The contents were mixed with a 20 μl pipette to ensure an even distribution of all components. The hydrogel mixture was then poured into an 18-well plate, each receiving 15 to 20 μl of the mixture. The gels were cross-linked under UV light for 5 minutes. After cross-linking, each well was filled with either neuron media or cancer media, depending on the cell type to be seeded on the scaffolds, to prevent the gel from drying out.

2.2.2 Cells in the PDMS microstructures

Cells were cultured in **bulk gels** and **PDMS microstructures** to study their motility and growth under controlled conditions. Two PDMS microstructures were employed: one with closed channels

and another with open channels. The closed-channel microstructure has a sealed top, allowing only axons to navigate through the channels. This poses a greater challenge for cell motility and necessitates a longer observation period for significant migration through the channels (Figure 7 a,c). The open-channel microstructure features a fully open top, facilitating cell growth and motility (Figure 7 b,d).

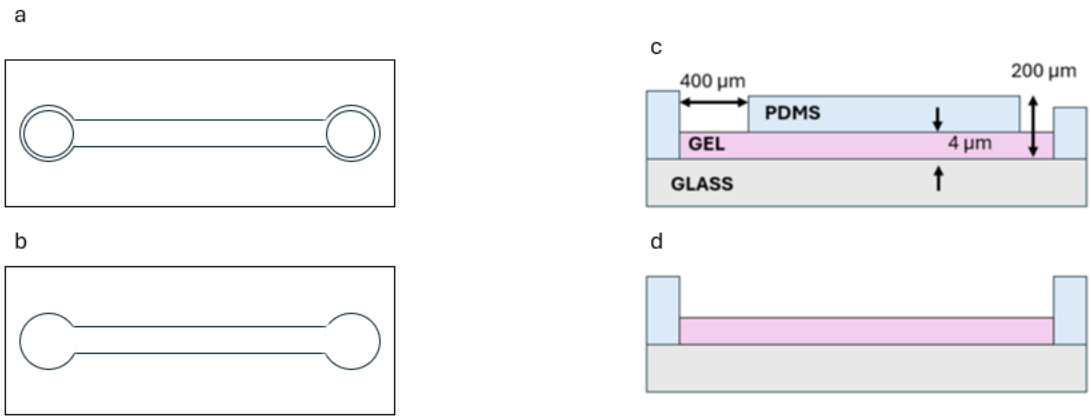

Figure 7: PDMS microstructure schematics. a,b Top view of the microchannels: The microchannels feature two wells. Gels are seeded inside the channel, and subsequently, neuron spheroids are placed in one well. After 21 days *in vitro*, GBM spheroids are seeded on the other side, **c: Side view microchannel closed on top:** The illustration shows the schematic of a closed microchannel. In this particular instance, the channel is sealed at the top with a PDMS layer, creating a 4µm opening that facilitates axon growth within the channel, while effectively preventing spheroid migration in the majority of cases, **d: Side view microchannel open on top:** This schematic depicts an open microstructure, specifically designed to facilitate cell growth. The morphology of this structure provides an entirely open environment resulting in uncontrolled cell migration along the channel.

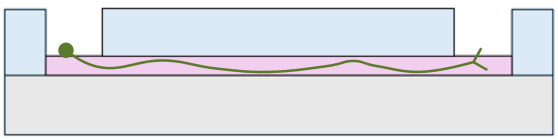

Figure 8: Neurons growing in the PDMS microstructure schematics. Side view of the neuron growing in the microchannel: Microchannels are filled with the hydrogel and then UV light crosslinked. After one day neurons spheroid are released on one side of the microchannel and after 21 days when they are fully matured glioblastoma spheroids are released on the other side.

To seed cells in the microstructures, we followed several steps. Ideally, the hydrogel was seeded inside the channels the day before, or at least 2 hours before cell seeding to eliminate all unreacted crosslinkers. However, a significant issue was that the hydrogel often spread across the entire microstructure instead of remaining confined to the channels. Consequently, this led to cells growing not only in the channels where the gel was seeded but also on top of the PDMS microstructures. This formation of large networks pulled cells outside the wells, subsequently affecting their controlled growth within the channels.

To address this concern, recent experiments have utilized a two-step coating process, utilizing both a polydopamine (pDA) and a polyvinylpyrrolidone (PVP) coating. This method has contributed to improved precision in gel seeding within the microstructures and has ensured more controlled

cell growth exclusively inside the microchannels..

pDA and PVP coating of PDMS microstructures

The microstructures were cut from the mask and transferred to a petri dish. pDA solution was then prepared by dissolving pDA powder in TRIS buffer (pH of 8.5) with a concentration of 2 mg/ml, and the mixture was vortexed. This solution was poured into the dish to completely cover the microstructures, which were then left in the solution for 2 hours, protected from light and airflow. Then the microstructures were rinsed five times with MQ water and left in MQ water. Then, a 2 mg/ml PVP solution was prepared by dissolving PVP powder in MQ water. After vortexing the mixture, the MQ water was removed from the dish before adding the PVP solution. The microstructures were then placed in the PVP solution for 4 hours, ensuring they were shielded from light and airflow. Subsequently, they were rinsed five times, alternating between MQ water and ethanol, and finally left in MQ water until seeding. One hour before seeding, the MQ water was completely aspirated, and the microstructures were allowed to dry thoroughly.

Meanwhile, Ibidi glass dishes were washed for 15 minutes with isopropanol and then rinsed five times with MQ water. Once the microstructures were sufficiently dried, both the microstructures and the glass dishes were plasma-activated for 1 minute to create a plasma bond between the PDSM microstructures and the glass dish. Then the hydrogel was introduced into the microstructure, commencing from one of the two wells within each microchannel (Figure 7 c,d). Subsequently, it was subjected to UV light for a duration of 5 minutes to initiate crosslinking. The following day, neuronal spheroids were seeded on one side of the microstructure (Figure 8).

2.2.3 Mechanical characterization

After fabrication, the hydrogels were characterized using two distinct methods to evaluate the differences in gel stiffness based on the weight percentage used in the gel mixture. These methodologies offer complementary insights into the material's mechanical properties, with one providing an overview of global properties and the other focusing on local mechanical characteristics.

Rheology

Rheological measurements are connected to the overall characteristics of the material. For this test, a gel was prepared in disc form by pouring 50 μl of the mixture between two glass slides and then crosslinking it under UV light for 5 minutes. Subsequently, the resulting disc was immersed in 2 ml of PBS and left overnight before the measurement to allow the gel to reach equilibrium with respect to liquid uptake. Mechanical properties were evaluated using a parallel-plate type rheometer, with the hydrogel disc positioned between the two plates(Figure 9).

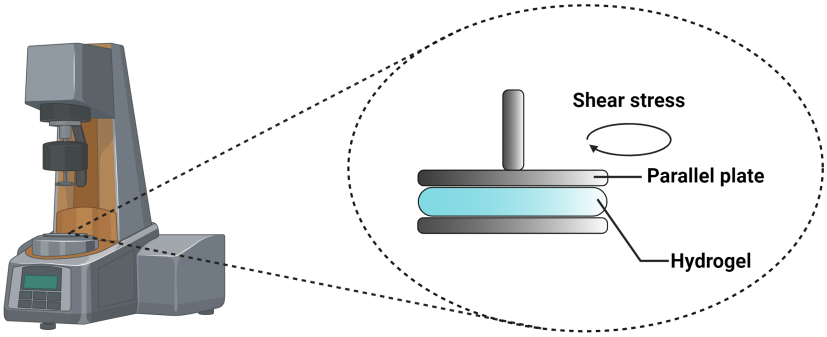

Figure 9: Rheometer schematics. For rheological measurements, the gel was shaped into a disk and positioned between two parallel plates. Subsequently, a shear stress with increasing magnitude was applied, and the resulting strain in the gel was recorded.

For this kind of characterization, a strain sinusoidal amplitude sweep ranging from 0.1% to 10% has been performed while keeping constant the frequency of the stress applied at 1 rad/s .

Fluid force microscopy

Fluid Force Microscopy (FFM) is a specialized form of atomic force microscopy with microchanneled cantilevers connected to a pressure controller [46]. The microchannel can be filled with an arbitrary liquid and this allows for 3D manipulation of living cells. In the case of interest, the FFM cantilever with spherical microbeads was used to perform micro indentation on the hydrogels to measure mechanical properties as shown in figure 10.

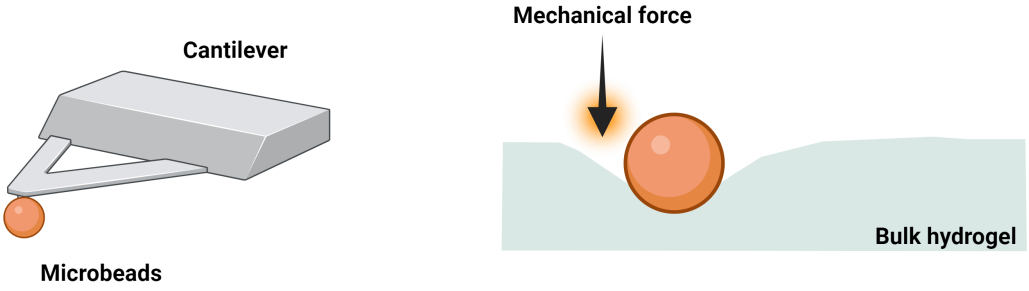

Figure 10: FFM schematics. The image depicts the configuration of the FFM, showing a cantilever with a microbead attached at its tip. This microbead is capable of deforming the hydrogel soft substrate through indentation.

For FFM measurements, hydrogel samples were prepared by applying 20-25 μl of the gel onto a glass coverslip that had been plasma cleaned for 2 minutes. This plasma treatment renders the glass surface hydrophilic, promoting uniform spreading of the gel. The gel on top of the coverslip was crosslinked under UV light for 5 minutes and then immersed in PBS overnight before testing. A probe with a stiffness (k in N/m) ranging from 0.1 to 0.9 N/m is typically selected to match the stiffness of the gels, suitable for measuring stiffness values between a few kPa and 100 kPa [46]. A similar approach is used when choosing the spherical tip. The tip's radius is determined based on the required spatial resolution, with a typical range of 10 to 250 μm for hydrogels. The analysis involves indenting multiple regions of the same sample, and Young's modulus is calculated from

the force versus indentation measurements using the Hertz model relation:

$$F = \frac{4}{3(1-\nu^2)} E\, \delta^{\frac{3}{2}} R^{\frac{1}{2}}$$

In the formula, F is the force, δ is the indentation, E is the Young's modulus, and ν is the Poisson's ratio taken as 0.5, assuming incompressibility.

2.2.4 Cell culturing

Human induced pluripotent stem cell (iPSC) derived neurons and primary glioma cells have been cultured in the hydrogel scaffolds.

Cell culturing: iNeurons

NGN2 iNeurons (Neuronal differentiation from iPSCs is initiated by the transcription factor Neurogenin 2 (NGN2)) were used in the form of 3D spheroids. They were typically placed on top of hydrogel scaffolds approximately one day after the gel preparation. When the gel preparation and seeding occurred on the same day, a minimum of one hour was allowed between gel formation and seeding. Additionally, the media was changed twice to remove any unreacted LAP.
Between 6 and 7 spheroids were visualized under an optical microscope, carefully picked up with a 10 μl pipette, and gently placed into each well on top of the gel. It was crucial to ensure that the pipette tip was submerged in the cell media without directly contacting the gel, to prevent any disruption to its structure.
To maintain cell viability, media changes were performed every 2-3 days, using only medium that was less than 2 weeks old. Before each media change, the medium was warmed to 37°C in a dry bath to ensure it was at the proper temperature for the cells. In each well, slightly less than half of the media, approximately 40 μl, was removed to account for evaporation, and around 60 μl of fresh media was then added. For maintaining iNeurons, a combined iNeurons-Glioma (CNG) medium was used. During the first 7 days *in vitro*, doxycycline (2 μg/ml) and laminin (3.2 μg/ml) were added to the complete CNG medium. From day 7 to day 10 *in vitro*, only laminin at the same concentration was added, and from day 10 onward, only the complete CNG medium was used for media changes as reported in the tables below:

Name	**Quantity**
Neurobasal Plus Media	500 ml
Glutamax	5 ml
Antibiotic Antimycotic 1X	5 ml
Sodium Pyruvate 1X	5 ml

Table 3: List of components for preparing 500 ml of CNG Medium Stock

Name	**Quantity**
CNG Medium Stock	50 ml
B27 Plus supplement (50X)	1 ml
N2 supplement (1000X)	0.5 ml
BDNF	50 μl
GDNF	50 μl

Table 4: List of components for preparing 50 ml of CNG Medium Complete

Time	Formula
Thawing and seeding	CNG + 10μl of RI (1:1000 diluition from stock: 1 μl RI in 1 ml CNG) + 2μl/ml Dox (1:500 diluition from stock: 2μl in 1 μl CNG
First medium change (about 1-2 hrs after seeding)	CNG + 2μl/ml Dox + 3.2μl/ml Laminin
Second medium change (after 24 hrs) to DIV7	CNG + 2μl/ml Dox + 3.2μl/ml Laminin
DIV7 to DIV10	CNG + 2μl/ml Dox
From DIV10	CNG

Table 5: List of components and their quantities added to the CNG Complete Medium based on the DIV

.

Laminin was first added to cold CNG, and then the complete media was warmed in a 37°C dry bath before being used to change the culture media.

Cell culturing: GBM

Primary glioma cells in the form of 3D spheroids, were typically placed on top of hydrogel scaffolds approximately one day after the gel preparation. When the gel preparation and seeding occurred on the same day, a minimum of one hour was allowed between gel formation and seeding, and the media was changed twice to remove any unreacted LAP as described for the neurons seeding 2.2.4. Between 6 and 7 spheroids were visualized under an optical microscope, carefully picked up with a 10 μl pipette, and gently placed into each well on top of the gel. It was crucial to ensure that the pipette tip was submerged in the cell media without directly contacting the gel to prevent any disruption to its structure. Also for cancer cells, media changes were performed every 2-3 days, using only a medium that was less than 2 weeks old. Before each media change, the medium was warmed to 37°C in a dry bath to ensure it was at the proper temperature for the cells. In each well, slightly less than half of the media, approximately 40 μl, was removed to account for evaporation, and around 60 μl of fresh media was then added. To maintain the cancer cells, Neurosphere Medium was used with the formulation detailed below:

Name	Quantity
Neurobasal Media	233.75 ml
DMEM/F12 1:1	233.75 ml
Non-Essential Amino Acids 1X	5 ml
Sodium Pyruvate 1X	5 ml
Sodium Bicarbonate 1X	2.5 ml
HEPES Buffer 25mM	12.5 ml
Glutaro/Max 1X	2.5 ml
Antibiotic Antimycotic 1X	5 ml

Table 6: List of components along with their respective quantities for preparing 500 ml of Neurosphere Medium Stock (Primary Tumor)

Name	Quantity
Stock Medium	10 ml
EGF	2 μl
FGF	8 μl
Heparin 1000X	10 μl
B27 without Vitamin A 50X	100 μl

Table 7: List of components along with their respective quantities for preparing 10 ml of Neurosphere Medium Complete

For co-culturing neurons with GBM spheroids, a different media formulation was used. Once the GBM spheroids were seeded into the neuron cultures, the medium was switched from Complete CNG to CNG+ as outlined below. The cancer growth factors, listed below, were added to the Complete CNG Medium:

Name	Quantity
EGF	2 μl
FGF	8 μl
Heparin 1000X	10 μl

Table 8: List of components along with their respective quantities for preparing 10 ml of CNG+ Medium

2.2.5 Immunohistochemistry

Immunohistochemistry (IHC) is a method used to detect specific molecules or proteins in tissue samples. This is done by using specific antibodies to bind to the antigens present in the tissue sections or cells. After culturing the samples for 30 days, they were fixed and then stained for primary and secondary antibodies to detect the specific proteins expressed by GBM cells.

Fixation

Cells were fixed before staining them, a crucial step for **preserving a snapshot of biological processes** as they occur in living organisms [47]. The fixation process **inactivates biochemical and proteolytic processes** and **immobilizes cell structures**, preserving their morphology and interactions.
In this particular case, the media solution was removed from each well of the 18-well plate, and each scaffold was covered with a 4% paraformaldehyde solution (PFA) and left for 15 minutes to allow the fixative to properly react with the cells' proteins.

PFA, being the **smallest aldehyde**, can be easily attached by a wide range of nucleophilic species of biological interest [47]. The carbon in the carbon-oxygen double bond (C=O) present in the aldehyde has a partially positive charge due to the higher electronegativity of the oxygen atom, making the carbonyl carbon an attractive site for nucleophiles. This interaction is fundamental to the **crosslinking process of proteins**. The fixation process by PFA is a two-step process:

- **STEP 1**: PFA reacts with a nucleophilic molecule (e.g., lysine group from a protein), forming a **covalent bond** resulting in a methylol adduct, which is then converted to a Schiff base by loss of a water molecule [48]
- **STEP 2**: The Schiff base reacts with another nucleophilic group, also from the same protein, **stabilizing the overall reaction** and completing the fixation process of the cells.

After treating the samples with PFA for 15 minutes, three 5 to 10-minute washes in PBS were done

to remove any remaining PFA. Subsequently, samples were stored in PBS covered with parafilm at 4°C to prevent evaporation until they were ready for staining.

Permeabilization

Before introducing the primary and secondary antibodies, the samples were **permeabilized**. This permeabilization step is crucial for **removing cellular membrane lipids**, which enables the large antibodies to enter the cells. It also impacts the nuclear membrane, making it suitable for targeting various cellular components [49].
Permeabilization typically involves two main types of reagents: organic solvents (e.g. methanol and acetone), which dissolve the lipid cell membrane, and detergents, which are amphipathic molecules such as saponin and Triton-X[49]. In this instance, Triton-X was used to lyse the cells.

Triton-X is a nonionic surfactant with a hydrophobic tail and a hydrophilic head. In aqueous solutions, Triton-X molecules form micelles, with the non-polar polymeric chains oriented inward to avoid contact with water, while the polar heads interact with the water. When Triton-X is added to a cell suspension, its hydrophobic tails interact with the hydrophobic inner layer of the cellular membrane, enabling it to **penetrate the lipid bilayer** and disrupt the interactions between lipid molecules within the membrane.

Primary and secondary antibodies

Antibodies are glycoproteins designed to bind with high specificity to a particular part of a target biomolecule, such as a specific protein sequence. While they offer precise binding capabilities, they may not detect high quantities of antigens on their own. To overcome this limitation and enhance detection sensitivity, signal amplification is employed using secondary antibodies. These secondary antibodies are labeled with a fluorophore or chromogen and are produced against the primary antibody's host organism. If the primary antibody was generated in rabbits, the secondary antibody would be anti-rabbit. As primary antibodies have been used:

- **Ki67**: It has been widely used as a protein marker for human tumor **proliferation** [50] . This protein is expressed throughout the entire cell cycle, **except** during the **G0 phase**, which is the resting phase when the cell is not actively dividing [50]. The cell cycle comprises four stages: G1 (gap 1), where the cell increases in size; S (synthesis), where DNA is replicated; G2 (gap 2), where the cell prepares for division; and M (mitosis), where the cell divides. The Ki67 protein is detectable at the nuclear level during all these phases but is rare or nearly undetectable in the G0 phase.
- **Nestin**: is a **cytoskeletal intermediate filament** initially characterized in neural **stem cells**, is now recognized to be present in cells with **progenitor and/or regulatory functions** [51]. Nestin plays a crucial role in cancer pathogenesis and is highly expressed in many tumors, such as gliomas [51]. It is also associated with cancer cell infiltration, **malignancy**, and migration, contributing to the enhanced ability of cancer cells to migrate and metastasize [51][52].
- **GFAP**: is an **intermediate filament-III protein** found specifically in **astrocytes** within the CNS, non-myelinating Schwann cells in the PNS, and enteric **glial cells** [53]. GFAP exists in multiple isoforms, which are different forms of the same protein that vary slightly in their amino acid sequences. The effectiveness of GFAP as a marker depends on these different isoforms, indicating that further research is needed. Initial studies have shown that GFAPα expression decreases in higher-grade gliomas, while GFAPδ levels remain relatively unchanged [53].

Staining procedure

- **Day 1**: All the PBS was removed from each sample, and a 0.1% Triton-X solution in PBS

was added. The samples were then incubated with this solution for 6 minutes before it was removed. Following this, the samples underwent six washes in PBS: the first three were 10 minutes long, while the last three were 5 minutes long, all performed in a blocking buffer (5% goat serum in PBS). After the washes, primary antibodies were added to the blocking buffer at a concentration of 1:500, and the samples were incubated overnight on a shaker at room temperature. The primary antibodies for the cancer samples were Ki67, Nestin, and GFAP.

- **Day 2**: After the primary antibodies were removed, the samples were washed six times with blocking buffer over 6-7 hours. Next, secondary antibodies were added in blocking buffer and incubated overnight on a shaker.
- **Day 3**: The secondary antibodies were removed, and the samples were washed twice with blocking buffer, with each wash lasting 10 minutes. Hoechst staining solution in PBS was then added to the samples and incubated for 1 hour. Following this, the samples were washed twice with PBS.

Figure 11 below provides a comprehensive depiction of the staining procedure.

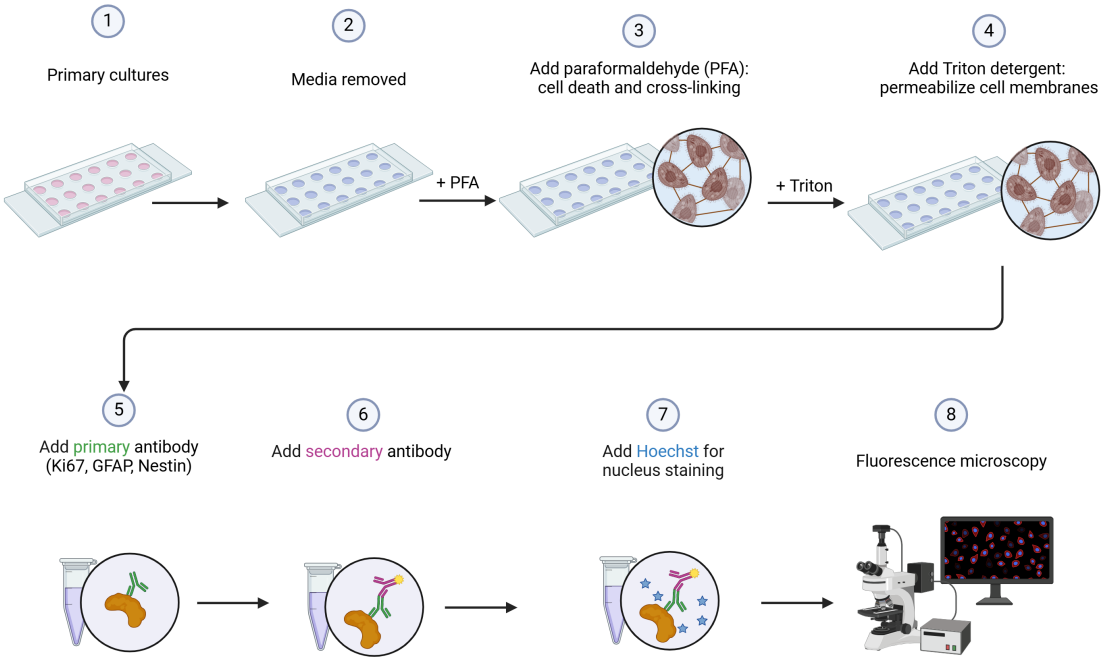

Figure 11: Immunostaining process. Immunostaining steps performed on GBM samples. Proliferating cells are marked by Ki67, indicating areas of high cancer cell proliferation. The cytoskeleton is highlighted with GFAP and Nestin staining, illustrating the expression of key structural proteins in the tumor cells.

Brain slices

Brain slices were prepared from primary tumor tissues directly resected from a patient. The tumor was initially cut into approximately 3 mm pieces, which were then thoroughly washed with an excess of PBS. Next, the pieces were immersed in 4% PFA until fully covered and left to fix in the refrigerator for 24 hours. After fixation, the samples were washed three times with PBS and stored in the refrigerator at -20 °C. From these fixed tumor pieces, 5 μm thick brain slices were sectioned using a microtome. The slices were mounted on glass slides, and the staining procedure was carried out directly on the slides. To contain the staining solution, a hydrophobic pen was used to draw circles around each brain slice and to protect the fluorescent molecules from photobleaching, a droplet of antifade reagent was added to each slice. A glass coverslip was then placed over the slice, and the prepared slides were stored in the -20 °C freezer overnight before imaging.

2.2.6 Stained GBM samples imaging and processing

After the staining process, GBM samples were imaged using a confocal laser scanning microscope (CLSM) equipped with a 20x objective to evaluate cancer proliferation and marker expression across different hydrogel stiffness levels. Z-stacks were captured to preserve the three-dimensional structure of the cells growing throughout the entire bulk of the gels. . The samples were focused on a specific focal plane, with acquisition start and end points recorded, continuing as long as cells remained visible across the different channels.
The CLSM used in this study was equipped with the following lasers, each selected based on the excitation requirements for the fluorescent dyes and antibodies. The table below lists each laser along with its corresponding characteristics, including gain, HV intensity, and offset:

Fluorescent marker	**Excitation Target**	**Gain, HV Intensity, Offset**
Hoechst 33342	nuclear DNA	1.0%, 400-450, 5%
Alexa Fluor 488	Ki67 antibody (visualizes specific cellular markers)	1.0%, 370-400, 5%
Alexa Fluor 555	Nestin antibody (labels neural progenitor cells)	1.0%,450-500, 5%
Alexa Fluor 647	GFAP antibody (labels astrocytes)	1.0%, 450-500, 5%

Table 9: Details of lasers used in the confocal microscopy, including excitation targets, gain, intensity and offset.

Following the acquisition, the images were processed using a customized Fiji code. Initially, the z-stack images were separated into individual channels as shown in figure 12, and each channel was then divided into separate slices.

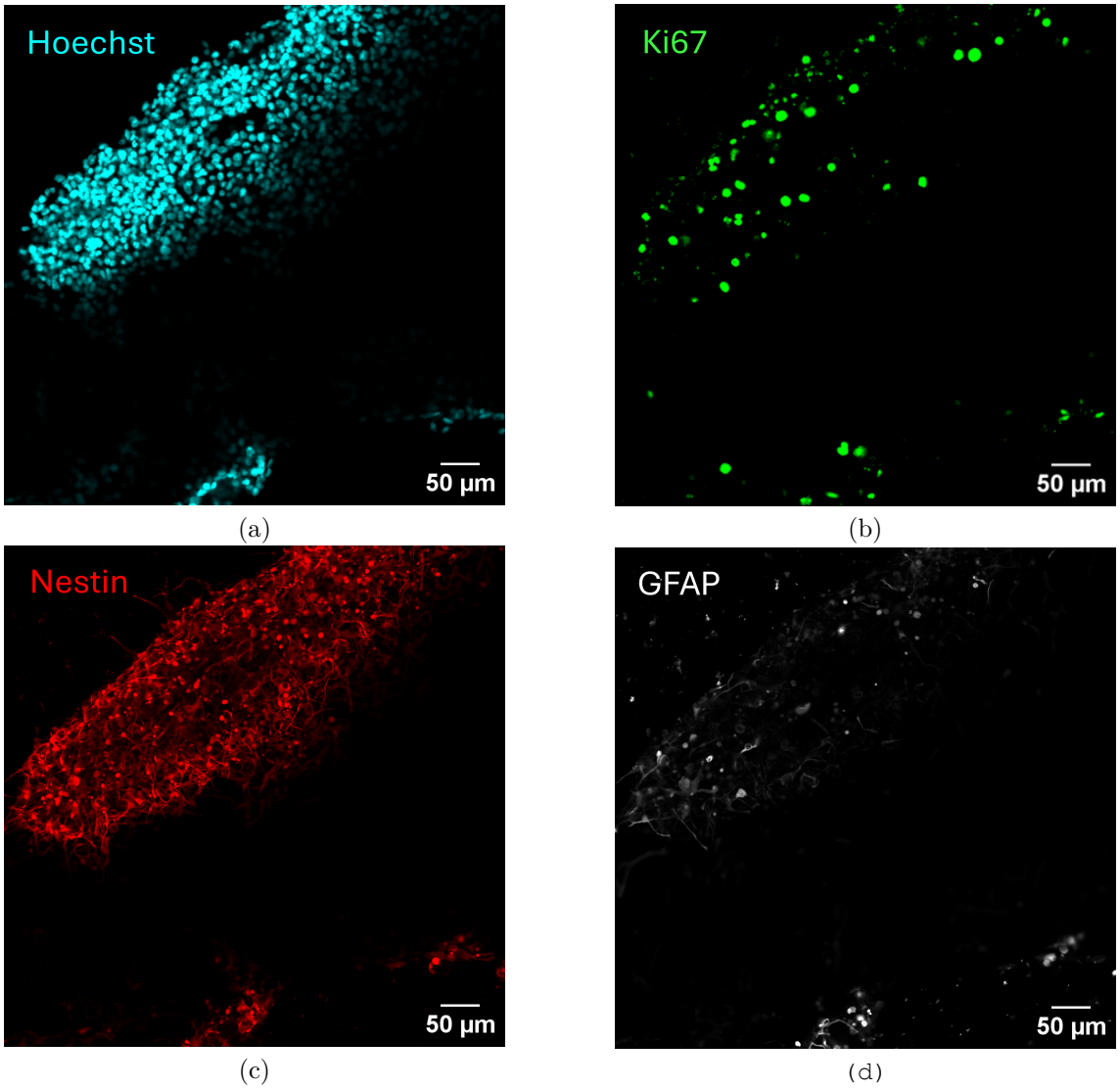

Figure 12: Image processing for GBM stained samples. The image shows the acquisition of four distinct channels: Hoechst (a) for the nuclei, Ki67 (b) for the proliferative cancer cell nuclei, Nestin (c), and GFAP (d) for the cell cytoskeleton.

The code was executed on each slice to assess cancer proliferation. Subsequently, the average proliferation rate was calculated across all analyzed slices to determine the overall proliferation rate.
The proliferation rate was determined by calculating the percentage of Ki67-positive nuclei relative to the total number of cells in various regions across multiple samples for each gel concentration. Since not all cells in the samples are actively proliferating, only a portion tested positive for the proliferation markers.
The total number of cells was determined using the Hoechst channel, which highlights nuclei. The total cell count corresponds to the number of nuclei identified in each slice. Simultaneously, the number of Ki67-positive cells was determined using the 488 nm excitation channel, which identifies proliferating cells.
In the analysis code, all regions of interest (ROIs) from both the Hoechst and Ki67 channels were recorded in the ROI manager array. For each Ki67-positive nucleus detected, it was verified whether the corresponding ROI overlapped with a nucleus (Figure 13).

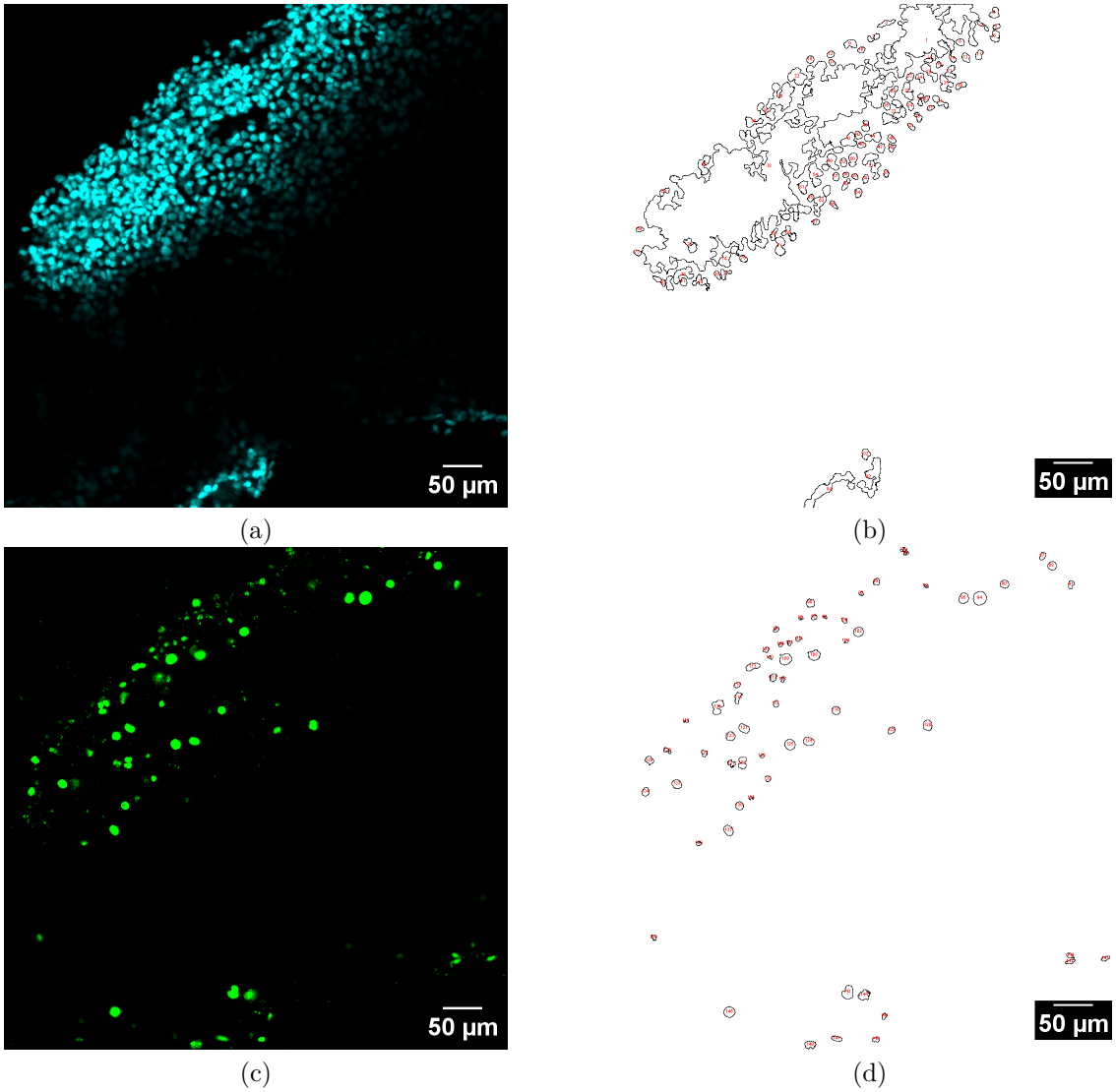

Figure 13: Hoechst and Ki67 rois. The image shows the identification of the region of interest from the Hoechst channel and the Ki67 channel, which is analyzed slice by slice. Following this, the detected particles are overlapped. (a) and (c) depict the original acquired pictures, whereas (b) and (d) show the detected particles delineated by the threshold operation.

To accurately assess the proliferation rate without overestimating it, specific measures were taken to ensure each Ki67-positive nucleus was counted only once as a proliferative cell. In densely packed regions, a single Ki67-positive nucleus could overlap with multiple nuclei; therefore, control was implemented to record the initial overlap upon detection and exclude any subsequent overlaps with other particles.
In examining the proliferation ratio in 3D, it was crucial to consider the growth behavior of GBM spheroids within the hydrogel matrix. As outlined in section 2.2.4, GBM spheroids were directly positioned on top of the hydrogel scaffolds. As a result, the cancer cells did not generally proliferate as **isolated cells or small clusters**, which would have aided in identifying overlapping particles. Instead, they proliferated as **intact spheroids, expanding their area**. This process was particularly noticeable in softer gels, where the spheroids lost their structural integrity and dispersed throughout the bulk gel in which they were embedded.

This growth pattern resulted in the formation of densely packed clusters of cancer cells on the gels. During image processing, particularly when using thresholding, these clusters were frequently identified as large aggregates rather than as distinct individual cells. Consequently, many cases where the tool identified a single particle actually corresponded to multiple cells.
To determine the percentage of proliferating cells, it was necessary to first calculate the **total number of cells** in each analyzed region. Since cells were clustered rather than proliferating individually, we estimated the total number of cells by measuring the **surface area of each particle detected** in the Hoechst channel. If the surface area of a detected particle exceeded the average cell nucleus size, we divided the detected area by the **average nucleus size** to estimate the total number of cells within each particle. This method allowed for an accurate calculation of the cell density and, subsequently, the ratio of proliferating cells to the total number of cells.
An additional measure was implemented to avoid underestimating cancer proliferation. This involved checking whether the particles detected in the Ki67-positive nuclei channel exceeded the average nucleus surface area. In some cases, multiple closely positioned Ki67-positive particles could be detected as a single larger particle. To address this, the total surface area of the detected particle was divided by the average nucleus size, ensuring a more accurate estimation of the proliferation rate.
The method used to calculate the proliferation rate was applied to both PDMS samples and brain slices. However, the images of brain slices, being primary tissues and captured at 10x magnification, exhibited some noise, which added complexity to the analysis. Specifically, when identifying nuclei and Ki67-positive nuclei, the minimum detectable particle size could be adjusted. These settings varied between channels because Ki67 often only stained parts of the nucleus, resulting in smaller positive areas. While it was possible to adjust the detectable particle size and improve specific areas by altering the image brightness to reduce noise, such adjustments could introduce bias into the analysis and result in incorrect assumptions.
When analyzing brain slices, a significant challenge we encountered was that the **Ki67 staining** often appeared scattered throughout the image, leading to the identification of large particles with surface areas exceeding the average nucleus size. However, it was crucial not to dismiss these particles outright as they could potentially indicate clusters of Ki67-positive cells. To ensure precise analysis, each detected particle was carefully evaluated to determine if the overlapping Hoechst-stained area fell within a similar size range as the Ki67-positive area. If the two areas were **comparable**, we calculated the total number of proliferating cells by dividing the Ki67-positive area by the average nucleus size. Otherwise, the particle was excluded from the proliferation calculation.

A similar method was used to evaluate GFAP and Nestin expression in cancer samples. The expression of GBM markers was assessed in two ways: first, by calculating the **average surface expression of these markers** to understand how **cells spread** on different substrates, and second, by determining the **percentage of cells positive for Nestin and GFAP** to examine how different substrates influence GBM cell differentiation. Both analyses were performed using a customized code in Fiji.
Images were acquired in z-stack form, and computations were carried out for each slice. An initial challenge, as discussed in section 2.2.4, was that cancer spheroids often did not proliferate as single cells or small clusters, resulting in large areas being detected as GFAP or Nestin positive. To address this issue and ensure accurate analysis, the z-stack images were separated into individual slices and each slice's channels were isolated.
Using a Fiji plug-in with the image calculator, an AND operation was performed between the Hoechst channel and the Nestin or GFAP channel (Figure 14), depending on the marker of interest. This operation highlighted only the pixels where the two channels overlapped. From this overlapping image, a particle analysis was conducted to measure the overall overlapping area, which was then divided by the average nucleus size specific to the gel being analyzed, resulting in the average number of cells positive for the marker.

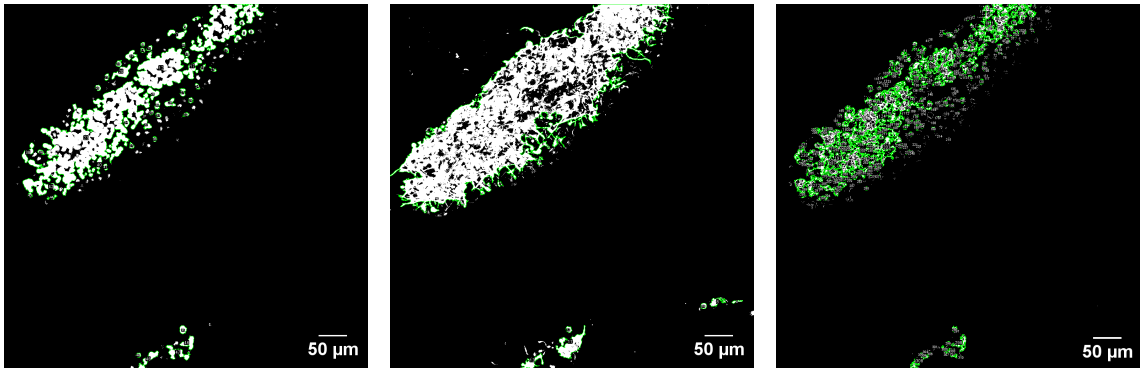

(a) (b) (c)

Figure 14: Methodology to evaluate the overlapping area between two different channels. The images illustrate the method used to compute the overlapping area between the Hoechst and Nestin or GFAP channels. Initially, the Hoechst channel was analyzed to calculate the total Hoechst surface area (a). This process was then replicated for the GFAP and Nestin channels (b). Subsequently, the channels of interest were superimposed, and the resulting image was analyzed to determine the overlapping area (c).

To compute the percentage of cells positive for a specific marker, this number was divided by the total number of cells detected in the slice. The Hoechst channel was used to detect the number of cells, and particle analysis was applied. If the detected particle area exceeded the average nucleus size, the total detected surface for each particle was divided by the average nucleus size to estimate the total number of cells.
For evaluating marker expression per cell to assess cell spreading, the average number of Nestin or GFAP-positive cells was calculated, and the total area covered by these markers was determined from the original images. This area was then divided by the average number of positive cells to obtain an index in μm^2 of cell spreading on the substrate. This analysis was performed slice by slice, and an average across all slices was computed to obtain the final value.

2.2.7 Neurons and GBM live imaging and processing

Neurons were repeatedly imaged to measure the rate of neurite growth on substrates with varying stiffness and to investigate the interactions between cancer cells and neurons on these substrates. Neurite growth was analyzed using z-stack imaging while maintaining a temperature of 37°C and ensuring the presence of CO_2. Images were captured by focusing on the neuron cell body, then recording the starting and ending focal planes by adjusting the focus until neurites were no longer visible under the confocal microscope. The step size for image acquisition was set between 1 and 2 μm to prevent any loss of information between focal planes according to the Nyquist limit. The initial analysis focused on three-dimensional neurite growth, examining preferences for specific focal planes and the impact of gel stiffness on growth through these planes. For the softest gels, it was hypothesized that reduced friction between focal planes would facilitate neuronal movement, potentially resulting in more complex neural structures and networks.

To assess neurite growth, we utilized a custom code to conduct a Sholl Analysis on each focal plane in Fiji. Sholl Analysis is a neuroscience technique used to measure the complexity of neuronal dendritic trees by placing concentric circles (Sholl rings) around the neuron soma at regular 1 μm intervals (Figure 15 a,b). This approach counts the intersections between dendrites and each ring, generating a plot of intersections per focal plane. The Sholl profile provides valuable insights into dendritic growth, showing the maximum number of intersections, the corresponding radius, and how intersections vary across focal planes.
To fulfill the project's objectives, we initially performed a Sholl analysis slice by slice to assess neurite growth across different focal planes. Subsequently, we carried out the same analysis on a z-projected image, ensuring that no information was lost when combining all slices into a single focal plane due to the small step size between focal planes.
For this analysis, we employed the Skeleton analysis plugin in Fiji to execute both a 2D Sholl analysis and a branching analysis as shown in figure 16. We merged all slices from the z-stack into a single focal plane. To enhance visibility, we applied mathematical logarithmic preprocessing, followed by thresholding, binarization, and skeletonization of the images.

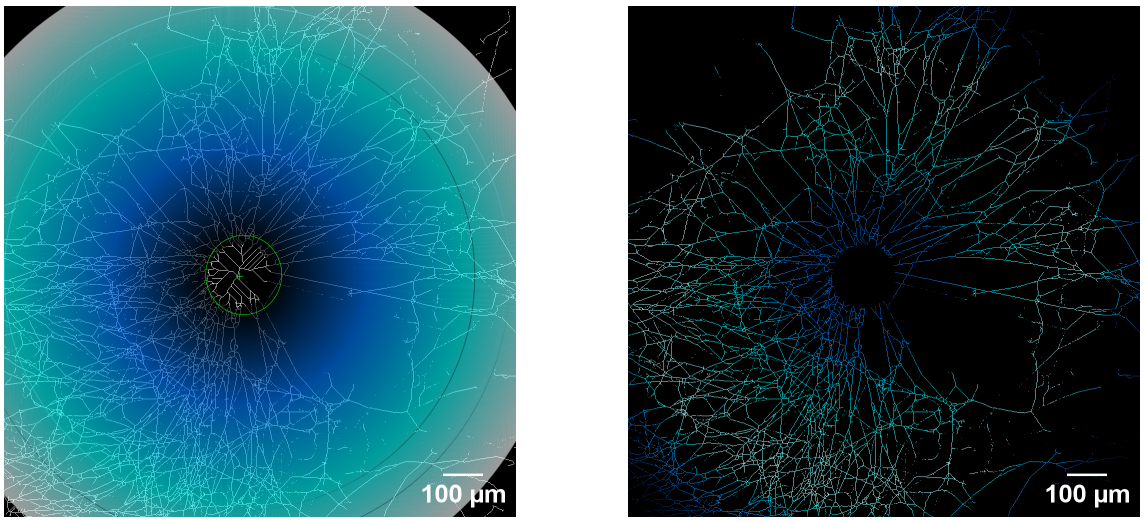

(a) (b)

Figure 15: Sholl Analysis. The image depicts the two steps involved in the Sholl Analysis. Firstly, concentric circles are sketched around the neuron's soma with an arbitrary step size (a). Subsequently, the intersections between the neurites and the concentric circles are identified, and the neurites are meticulously traced (b).

Skeletonization simplified the **axons and neurites** to **single-line structures**, facilitating easier computation of the neurite network. This process revealed various details about the neurite network, including the **number of branches**, which are segments connecting end-points, end-points to junctions, or junctions to junctions. It also provided counts of different types of voxels, such as end-points, slabs, and junctions. Junctions were analyzed to identify merging points, as well as triple and quadruple points where three or four branches converge.

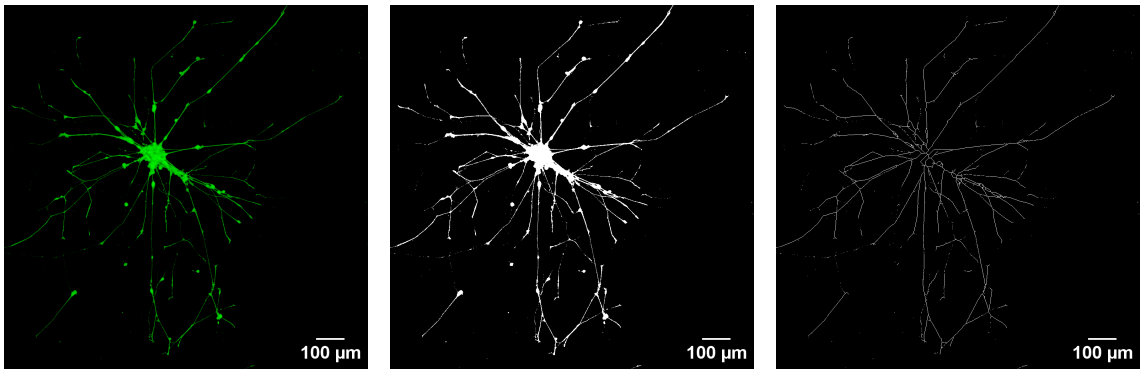

(a) (b) (c)

Figure 16: Skeletonization process. The images provide a visual representation of the skeletonization process: (a) the original image of the GFP-positive neuron, (b) the thresholded image, and (c) the skeletonized image with neurites and axon reduced to lines.

2.2.8 GBM motility

To access cancer motility on different substrates and in different conditions, after 21 days (the necessary time to wait for neurons to be completely mature), GBM spheroids were seeded both on the bulk gels and in the PDMS microstructures and the samples were imaged over time to monitor cancer growth and motility towards the neurons.
Images were acquired in timelapse mode, with each frame processed individually. In Fiji, the Manual Tracker plug in Cordelières, 2005) was used to analyze cell trajectories and measure their velocity over time. To perform this analysis, the centroid of the GBM spheroid or single cell was focused, and the center was manually tracked slice by slice. The velocity over time was then evaluated based on the tracking and automatically computed in Fiji.

3 Results

3.1 Mechanical characterization

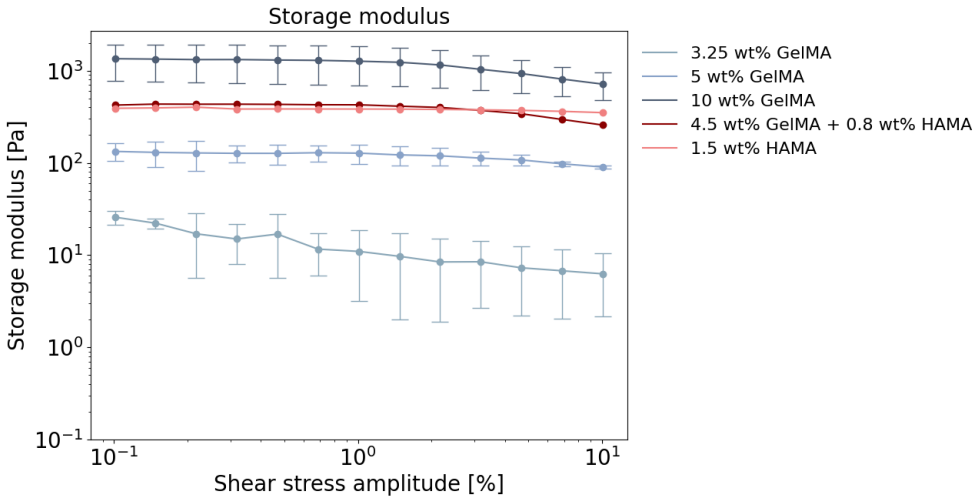

Figure 17: Storage modulus. The graph displays the storage modulus results for different weight concentrations of GelMA and HAMA. Lower weight concentrations of gels show reduced elasticity and stiffness. Including HAMA in the gel formulation increased the Young's modulus compared to 3 and 5 wt% GelMA-only hydrogels. This indicates that HAMA is effective in stiffening the gels.

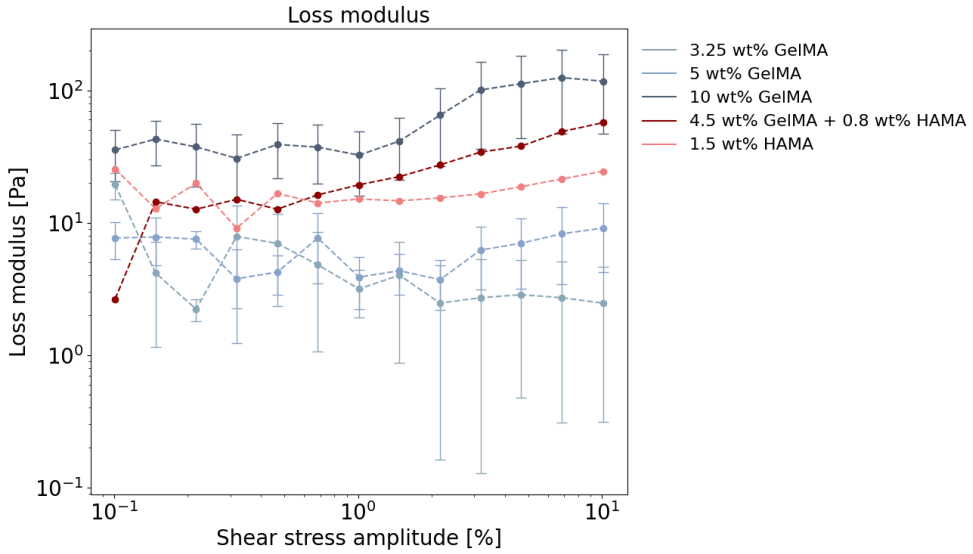

Figure 18: Loss modulus. The graph presents the results for the loss modulus of various weight concentrations of GelMA and HAMA as measured by the rheometer. The loss modulus is a parameter that provides insight into the viscoelastic properties of a material. When analyzing the elastic region at this specific shear stress amplitude, it is noted that the loss modulus is lower than the elastic modulus, indicating that the material is still within the elastic range. As stress increases, there is an observed rise in the loss modulus, signifying that the material is undergoing a viscoelastic transition.

Rheological assessments have been executed to analyze the characteristics of GelMA at various weight percentages (3 wt%, 5 wt%, and 10 wt%), as well as the GelMA + HAMA composite at a composition of 4.5 wt% GelMA + 0.8 wt% HAMA, alongside HAMA at a weight percentage of 1.5 wt%. These evaluations aim to elucidate the elasticity and liquid-like properties linked to polymer concentration and chemical composition. The results clearly demonstrate that a **higher polymer concentration** leads to an increase in the **storage modulus's value** (Figure 17), indicating that the material becomes stiffer as the polymer concentration increases. To assess the material's stiffness, the storage modulus value was measured at **0.1% strain amplitude**. At this point, the material's stiffness is determined solely by G', confirmed by the corresponding tanδ value at the same strain level below 1. For a shear strain of 0.1%, the values obtained for different polymer concentrations and compositions are presented in the table below:

Hydrogel composition	**Rheological Properties**		
	G' (Pa)	**G" (Pa)**	**tanδ**
GelMA 3 wt%	25.78	19.39	0.74
GelMA 5 wt%	133.249	7.66	0.06
GelMA 10 wt%	1348	35.51	0.06
GelMA 4.5 wt% + HAMA 0.8 wt%	423.3	2.65	0.006
Hama 1.5 wt%	390.91	.25.44	0.065

Table 10: Rheological properties of different hydrogel compositions measured at various polymer concentrations with a strain amplitude of 0.1% and constant frequency.

As presented in the table, the storage modulus's value increases from the softest GelMA formulation (3 wt%) to the stiffest composition (10 wt%), including the GelMA-HAMA composition discussed in section 1.5.3. At this strain amplitude, all the gels are in their elastic region, indicated by a tanδ value **below 1**. However, the softest concentration still exhibits a higher tanδ value (around 0.7) compared to the stiffer gels, suggesting that this softer formulation requires a much lower strain amplitude to undergo the viscoelastic transition (Figure 18). The findings also demonstrate that HAMA significantly **enhanching the stiffness of gels**. For instance, a formulation containing 4.5 wt% GelMA and 1 wt% HAMA achieves a Young's modulus of approximately 400 Pa, which is more than twice that of a gel with 5 wt% GelMA alone. Furthermore, a formulation with 1.5 wt% HAMA also exhibited a Young's modulus roughly double that of the 5 wt% GelMA gel when tested with a rheometer.

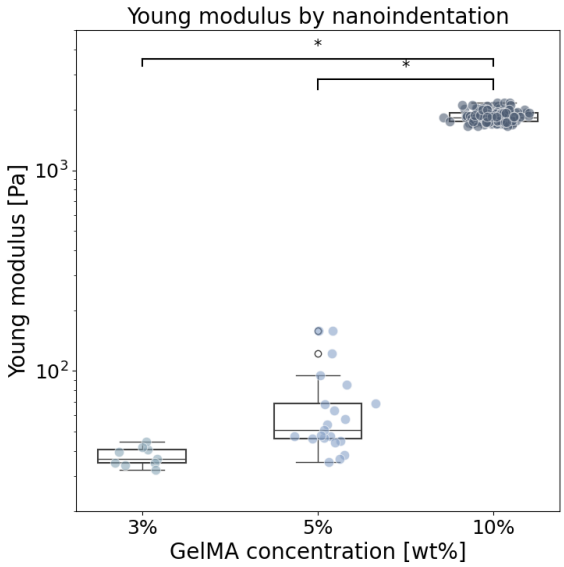

Figure 19: Fluid Force Microscopy measurements of the hydrogels' Young's modulus. The graph illustrates the measurements of the Young's modulus of hydrogels using nanoindentation with FFM. Similar to rheology, an increasing trend in gel stiffness is observed with an increasing gel wt% concentration, $*p$ value < 0.0001 between 3 wt% and 10 wt% and 5 wt% and 10 wt% evaluated with ANOVA test and the post-hoc Tukey's multiple comparisons test. FFM measurements, focusing on local properties, do not completely align with rheology, which examines global mechanical properties. This allows FFM to capture local changes in stiffness that rheology may not detect.

The FFM analysis involved using nanoindentation to measure the indentation depth in various regions of the same hydrogel sample in relation to the applied force. The trend of the FFM analysis align with the assumptions and rheology results, demonstrating that a higher polymer concentration correlates with an increased Young's modulus and overall stiffening of the matrix. However, the plotted absolute values reveal significant deviations from the rheological analysis. Specifically, the Young's modulus for the 10 wt% and 5 wt% GelMA formulations approximates 2 kPa and 0.05 kPa, respectively, diverging from the rheology results indicating values of approximately 1.3 kPa and 0.1 kPa for the respective formulations.

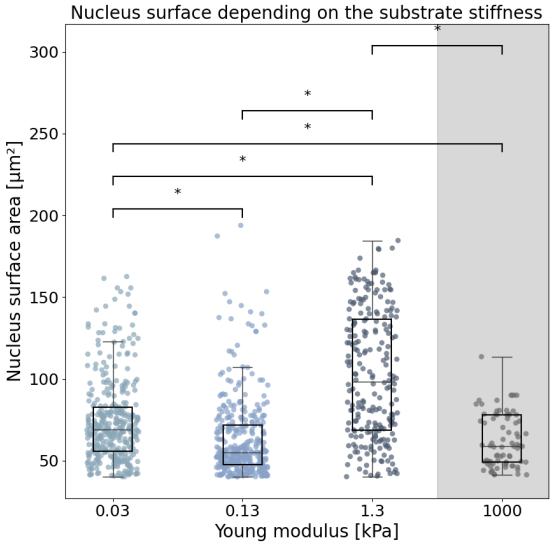

Figure 20: Nuclear Surface: The plotted data shows the average nuclear surface area relative to various substrate stiffness levels. Typically, for hydrogels, the nucleus surface area increases as the substrate becomes stiffer, $*p\text{value} < 0.0001$ between 0.03 kPa and 0.13 kPa, 0.03 kPa and 1.3 kPa, 0.03 kPa and 1000 kPa, 0.13 kPa and 1.3 kPa and 1.3 kPa and 1000 kPa, computed from the Kruskal-Wallis and post-hoc Pairwise Mann-Whitney U test. However, for glass samples, this trend is not consistent. Further analysis involving marker analysis for staining cytoskeletal markers is essential for a more comprehensive understanding.

For the aims of this project, the surface area of the cell nucleus was accessed to determine the average nucleus size, which was essential to calculate the proliferation ratio of cancer cells under varying gel conditions. To accurately evaluate the spreading of cell nuclei on different gels, multiple regions and samples from different stock solutions were examined. This analysis revealed significant variability in the nucleus area within the same samples. However, the mean values and the observed trend between soft and stiff gels remained consistent and reproducible. The nuclei size was also assessed in cancer samples grown PDMS microstructures, showing a contrasting pattern compared to the hydrogels . Instead of an increase, a decrease in nucleus size was observed, despite the higher Young's modulus of PDMS relative to the stiffness of the hydrogels. Specifically, the average nucleus area ranges from approximately 105 to 80 μm^2, progressing from the most rigid to the most flexible gel substrate. For the samples cultured on PDMS microstructures, the average nucleus surface measures around 70 μm^2 Figure(20).

3.2 GBM marker expression

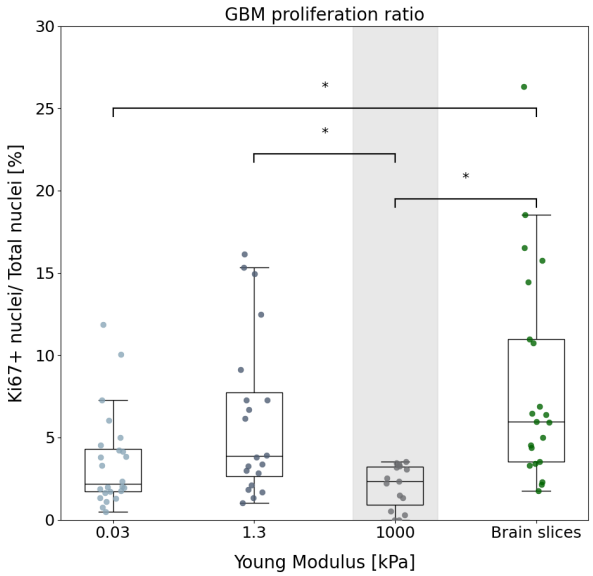

Figure 21: GBM cells proliferation ratio. The figure depicts the proliferation ratio of GBM cells in relation to varying hydrogel stiffness, comparing their growth in 2D culture on PDMS microstructures and human brain slices, $*p$ value 0.005 between 0.03 kPa and brain slices, 0.03 between 1.3 kPa and 1000 kPa and 0.00031 between 1000 kPa and brain slices computed from the Kruskal-Wallis and post-hoc Pairwise Mann-Whitney U test. The results reveal variability in proliferation across the same sample, with stiffer gels promoting higher proliferation in cancer cells. Cultures on glass, instead, demonstrate a lower proliferation ratio as well as lower variability.

The Ki67 immunohistochemistry was performed to evaluate cancer proliferation across varying stiffness levels. Specifically, the study involved analyzing scaffolds derived from different stock solutions and from multiple regions within a single scaffold. The findings from the gels and 2D samples were compared, considering that the cells analyzed originated from the same patient. However, in the case of the brain slices, a different patient was involved, necessitating a focus just on intertumoral variability, as proliferation is influenced by both the mechanical characteristics of the microenvironment and patient-specific factors. The results confirmed that **stiffer substrates** enhance **cancer proliferation**, with an average proliferation rate of 6.4% compared to 3.4% in softer gels. The proliferation rates within the gels exhibit a **general increase** in comparison to the results derived from **2D cultures on PDMS**, where the average proliferation rate stands at 2%. Moreover, it is important to note that there is a higher degree of variability in the outcomes for gel samples compared to 2D samples. This observation suggests that gels may more accurately mimic **intratumoral heterogeneity**, similar to brain slices. (Figure 21).

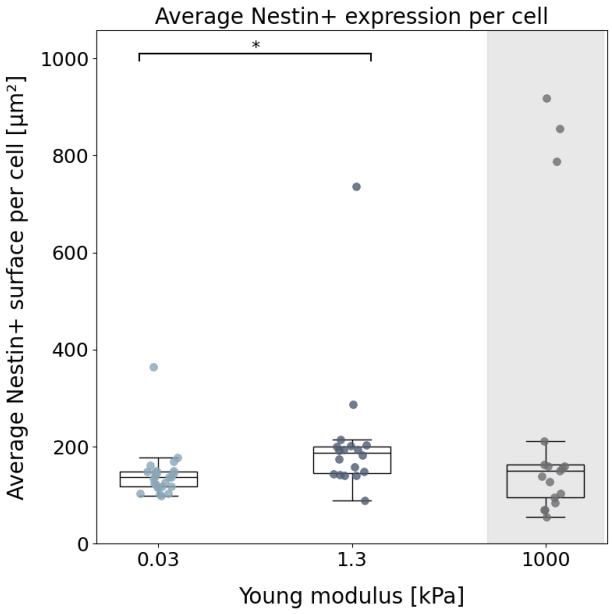

Figure 22: Nestin positive surface expression. The graphic displays the average surface area of Nestin-positive cells in relation to the stiffness of the substrate for different types of gels, as well as samples cultivated on PDMS. The findings indicate that the average surface area increases as the substrate's stiffness increases, $*p$ value 0.002 between 0.03 kPa and 1.3 kPa computed from the Kruskal-Wallis and post-hoc Pairwise Mann-Whitney U test, suggesting that cells spread more extensively on firmer gels, resulting in a larger overall surface area.

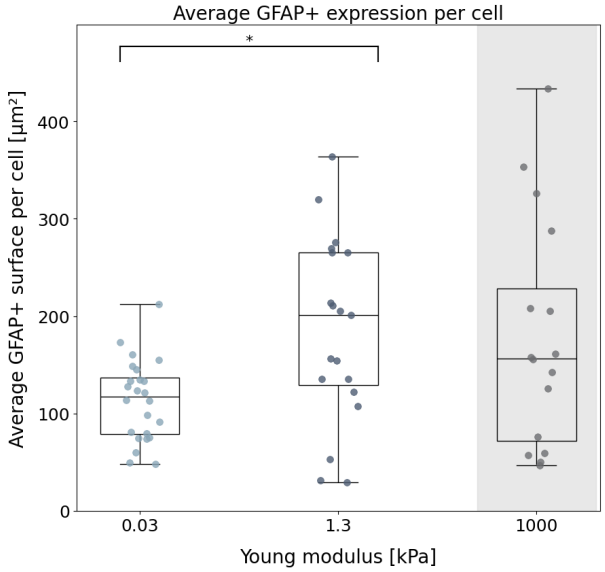

Figure 23: GFAP positive surface expression The graph illustrates the average surface area of GFAP-positive cells in relation to the substrate stiffness for different gel types, as well as samples cultured on PDMS. The results indicate that the average surface area increases with the stiffness of the substrate, suggesting that cells spread more on stiffer gels, $*p$ value 0.02 between 0.03 kPa and 1.3 kPa computed from the ANOVA test and post-hoc Tukey's multiple comparisons test

In this study, an analysis was conducted to examine the influence of substrate stiffness on cell spreading. Nestin and GFAP immunohistochemistry were utilized to assess cells derived from the same patient. These cells were subjected to culture on two different gel concentrations and PDMS microstructures. Specifically, for the gel samples, the cells were cultured on multiple scaffolds obtained from different stock solutions. Subsequently, various regions of the same samples were analyzed to consider both the variability in gel fabrication resulting from differences in the stock solution and the diversity in mechanical properties across distinct regions within the same scaffold. The findings demonstrate that irrespective of the nucleus spreading on the gel scaffolds based on their stiffness, there is an observed increase in the average Nestin and GFAP positive surface with the rise in substrate stiffness in cancer samples. On the softest substrates, the values are approximately 140 μm^2 for Nestin and 113 μm^2 for GFAP. Conversely, on the stiffer gels, the average positive surface for GFAP and Nestin is 208 μm^2 and 185 μm^2, respectively. In 2D cultures on PDMS, the results indicate 253 μm^2 for Nestin and 177 μm^2 for GFAP.

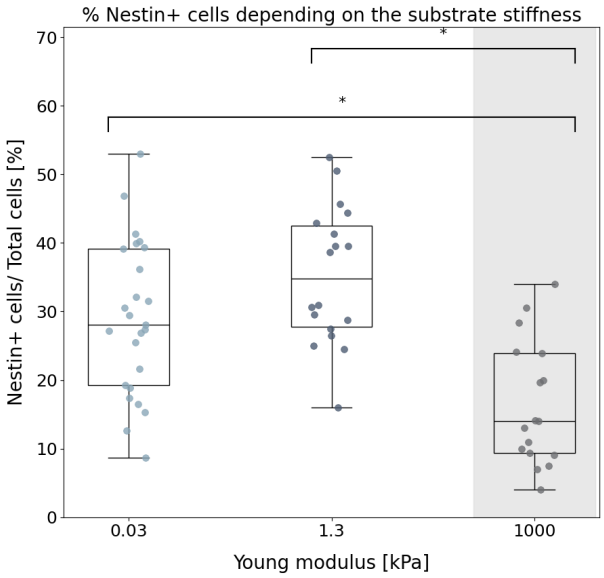

Figure 24: Nestin positive cells percentage. The graph depicts the percentage of Nestin-positive cells for the softest and stiffest concentrations of GelMA, as well as samples cultured on PDMS. The results conclusively demonstrate that stiffer gels promote a higher expression of Nestin, which aligns with an increased proliferation ratio of cancer cells on stiffer substrates, $*p$ value 0.0008 between 0.03 kPa and 1000 kPa and <0.0001 between 1 kPa and 1000 kPa computed from the ANOVA and post-hoc Tukey's multiple comparison test. Furthermore, the data indicates that the percentage of Nestin-positive cells on gels exceeds that observed on PDMS, suggesting that marker expression is influenced by both the mechanical and chemical properties of the cell culture environment.

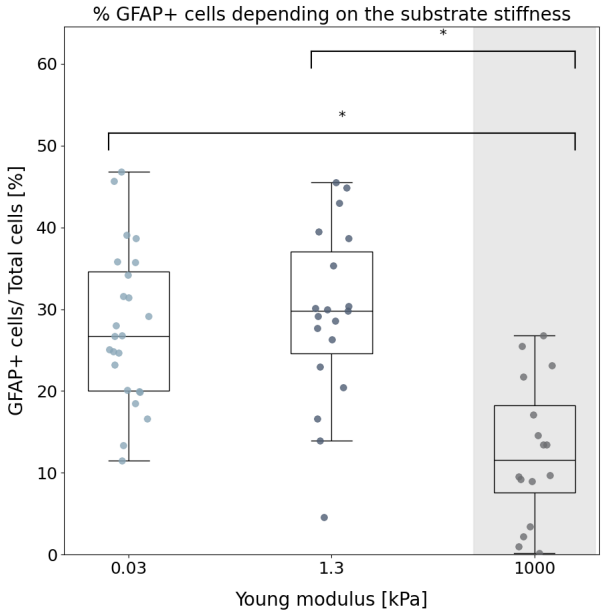

Figure 25: GFAP positive cells percentage. The graph depicts the percentages of GFAP-positive cells for the softest and stiffest concentrations of GelMA, as well as samples cultured on PDMS. The results suggest that there is only a 1% difference in the percentage of GFAP-positive cells between the stiff and soft concentrations, indicating similarity between the two different conditions, $*p$ value <0.0001 between 0.03 kPa and 1000 kPa and 1.3 kPa and 1000 kPa, computed from the ANOVA and post-hoc Tukey's multiple comparison test. This implies that GFAP may not be a specific enough marker to assess GBM aggression. Percentage is still higher compared to samples cultured on PDMS.

The study employed Nestin and GFAP immunohistochemistry to assess tumor malignancy and stemness by quantifying the percentage of Nestin and GFAP-positive cells on diverse substrates. Analysis was performed on cells from the same patient to establish a correlation between proliferation (ki67 immunohistochemistry), tumor malignancy, and stemness. Furthermore, the study took into account the variability in the mechanical properties of gels by analyzing cells growing on scaffolds derived from different stock solutions and multiple regions within the same scaffold for each sample. The data reveals that on stiffer substrates, the percentage of Nestin and GFAP positive cells is 35% and 29% respectively, while on softer substrates, these percentages are 29% and 27% correspondingly. This indicates a slightly higher expression of the Nestin marker on stiffer substrates, with less disparity in GFAP expression. A comparison with the 2D cultures on PDMS demonstrates a more pronounced variance. In the 2D cultures, the percentage of Nestin and GFAP positive cells is 16.4% and 12.5% respectively, lower than the percentages observed for the hydrogel scaffolds.

3.3 Neurons analysis

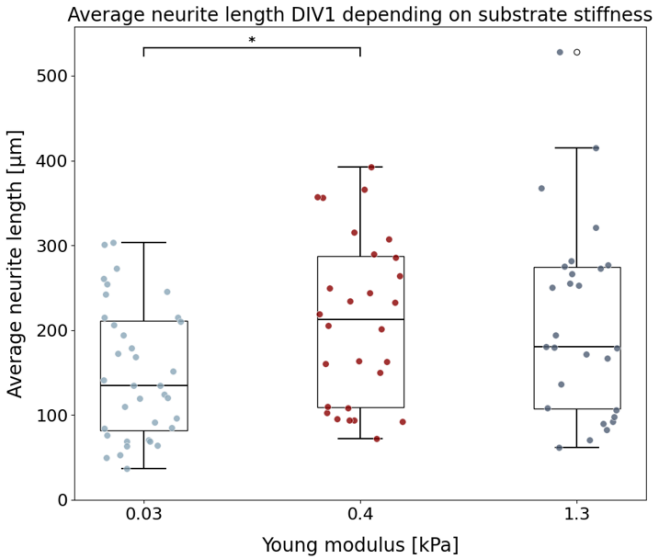

Figure 26: Neurites average length DIV1. The plot illustrates the average length of neurites after 24 hours based on the gel stiffness. The data indicates that in the initial phase of neuron growth when neurons have not yet started branching, stiffer substrates tend to promote better axon and neurite elongation, $*p$ value 0.032 between 0.03 kPa and 0.4 kPa computed from the ANOVA and post-hoc Tukey's multiple comparison test.

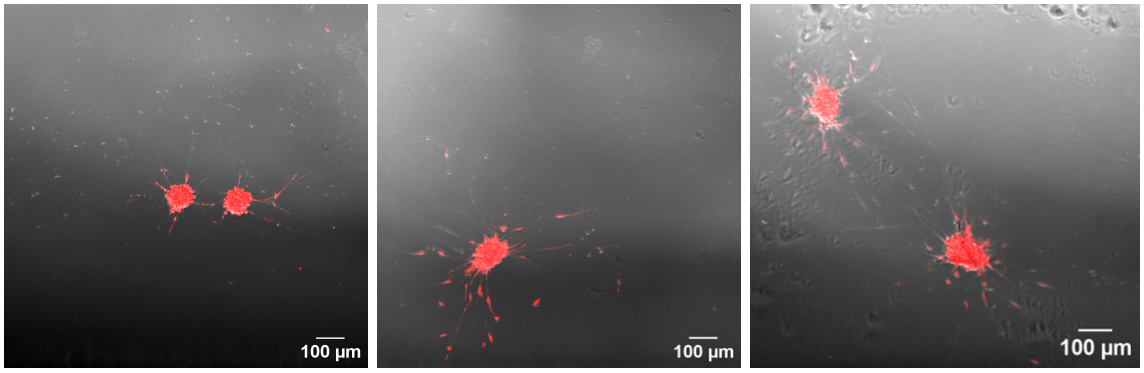

(a) (b) (c)

Figure 27: NGN2 RFP neurons DIV1. The images provide a visual representation of the neurons at the first DIV for different substrates stiffnesses and chemical compositions: (a) 3 wt% GelMA - 0.03 kPa, (b) 4.5 wt% GelMA + 0.8 wt% HAMA - 0.4 kPa, and (c) 10 wt% GelMA - 1.3 kPa.

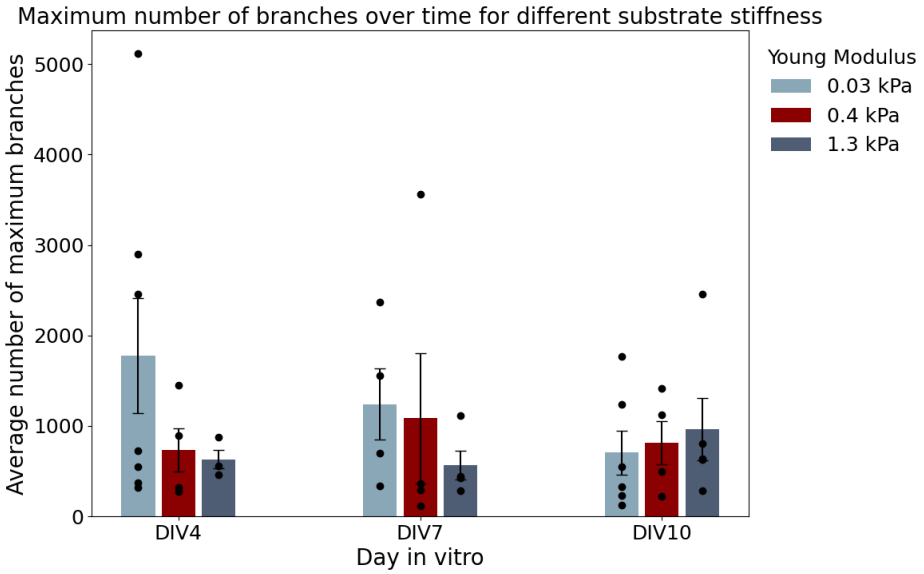

Figure 28: Average number of maximum number of branching at different time points. The graph illustrates the average maximum number of branches at different time points for three distinct gel formulations. The results indicate substantial variation in the maximum number of branches during the initial 10 days of incubation. This variability stems from averaging results across different cells and batches, as well as the inherent variability within the same batches, leading to differential growth patterns and delayed onset of growth in some spheroids.

To characterize how substrate stiffness affects neurite growth and branching in bulk gels, NGN2 RFP positive neurons were cultured on soft GelMA-based gels (3 wt%, corresponding to Young's modulus of around 30 Pa) and on stiffer hydrogel scaffolds (10 wt% GelMA, corresponding to Young's modulus of around 1.3 kPa), as well as GelMA-HA hydrogels (4.5 wt% GelMA and 0.8 wt% HAMA corresponding to Young's modulus of around 400 Pa) (Table 10) (Figure27). Neurite length was assessed at DIV1 (day 1 *in vitro*), and the average length was computed. The findings reveal that neurite length is notably greater on firmer substrates in comparison to more compliant ones. Specifically, the softest substrate exhibited an average neurite length of 150 μm, while the stiffest substrate demonstrated an average neurite length of 250 μm. Calculations were carried out to determine the maximum number of branches for multiple neurons cultured on various gel substrates derived from different stock solutions. These neurons were evaluated at different time points to observe changes across the substrates over time. The initial count of branches on the first day was zero, as indicated in section 4.3, as neurons primarily extended their dendrites rather than branching.

The neurons were assessed at DIV4, DIV7, and DIV10. From day 4 *in vitro*, the neurons displayed increasingly intricate branching. On softer substrates, the number of branches exceeded 1500, while on stiffer substrates, it reached just above 500 (Figure 28). However, the trend was inconsistent over time, suggesting that branching did not uniformly increase across different conditions.

3.4 GBM motility

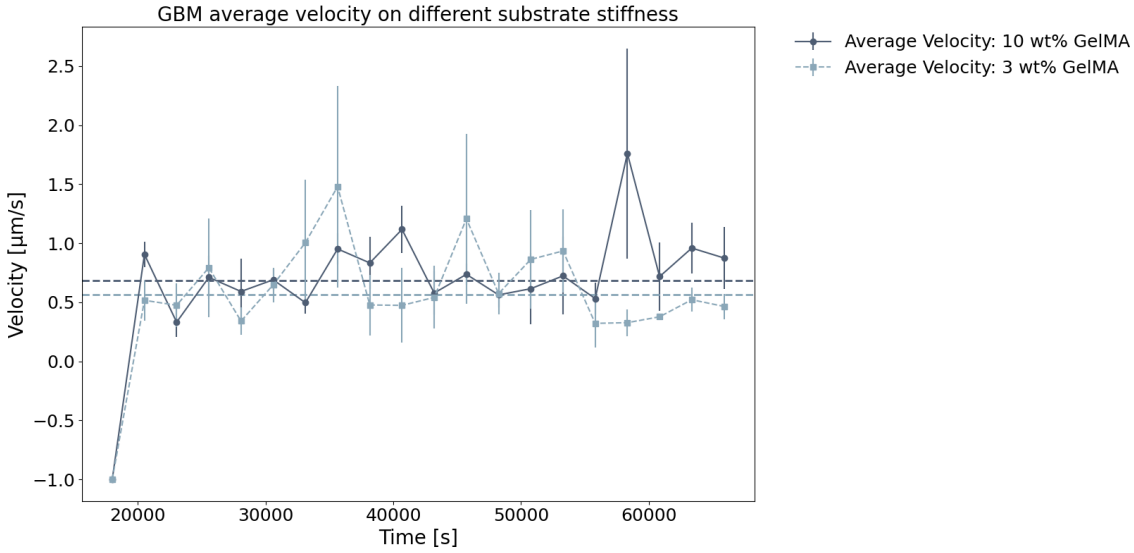

Figure 29: GBM spheroids average velocity on different GelMA stiffness. The graph depicts the average velocity of GBM spheroids on 3 wt% and 10 wt% GelMA. The analysis involved assessing the trajectory and velocity of multiple spheroids on different gel scaffolds. The findings suggest that the average velocity is slightly higher on stiffer substrates, average velocity on 10 wt% GelMA 0.69 μm/s, average velocity on 10 wt% GelMA 0.57 μm/s.

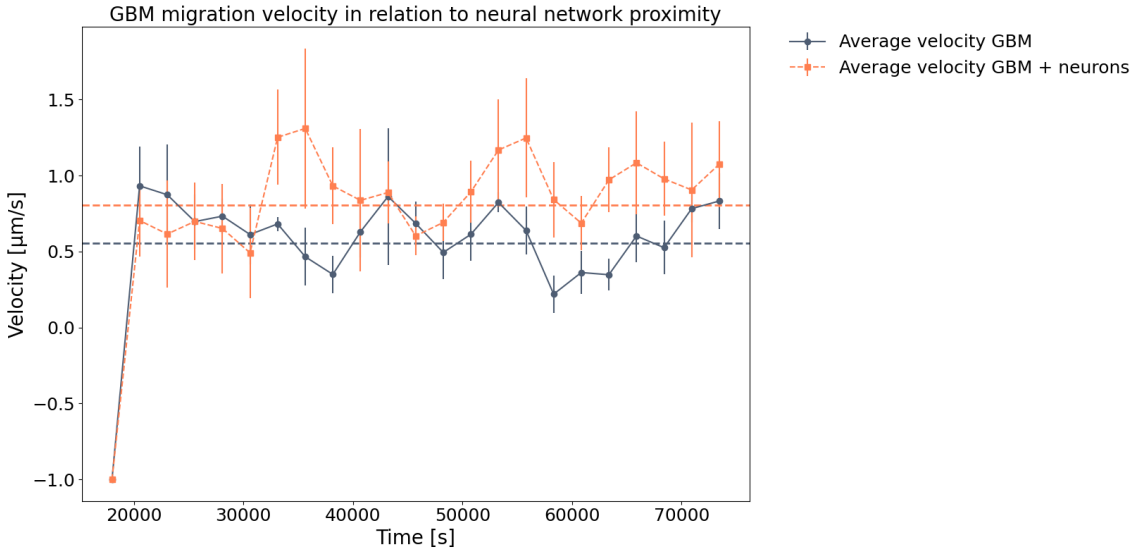

Figure 30: GBM spheroids on 10 wt% GelMA average velocity in the proximity of neural networks and afar. The graphical representation illustrates the average velocity of GBM spheroids cultured on 10 wt% GelMA. The findings demonstrate that the velocity of GBM spheroids is higher when the cells are in close proximity to neural networks, with an average velocity of 0.806 μm/s rather than if they are far away from them with an average velocity of 0.55 μm/s. This indicates that the interaction between neurons and cancer cells augments GBM migration.

The average velocity of GBM spheroids was determined on substrates comprising 10 wt% and 3 wt% GelMA. The analysis involved calculating the average velocity for each time point based on the velocities of all spheroids considered, resulting in increased variability in the findings. However, it is important to note that the velocity is influenced by various factors, with proximity to neurons being particularly significant. The average velocity of GBM spheroids was assessed for spheroids in close proximity to neurons, as well as for spheroids randomly seeded within the gels where the neuron network was not diffused for 10 wt% GelMA only hydrogels, due to a larger quantity of regions of interest (ROIs). As indicated in figure 30, spheroids in the proximity of the neural network demonstrated higher average velocities, suggesting that neurons enhance the migration and motility of GBM spheroids.

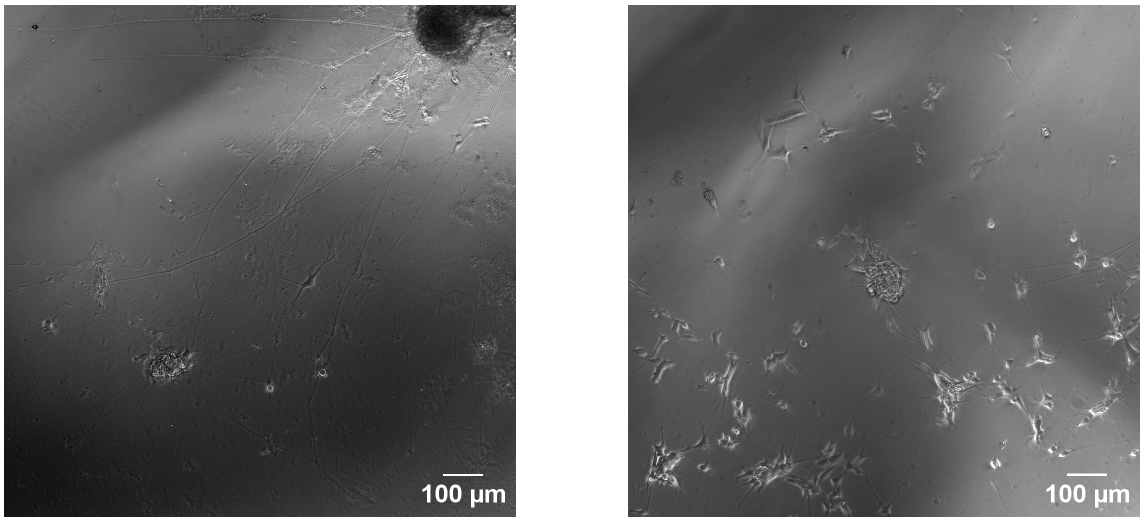

(a) (b)

Figure 31: GBM and neurons networks on different substrate stiffnesses at DIV2. The images depict the migration of individual cells in response to varying levels of gel stiffness: (a) GBM spheroid on 3 wt% GelMA, (b) GBM spheroid on 10 wt% GelMA.

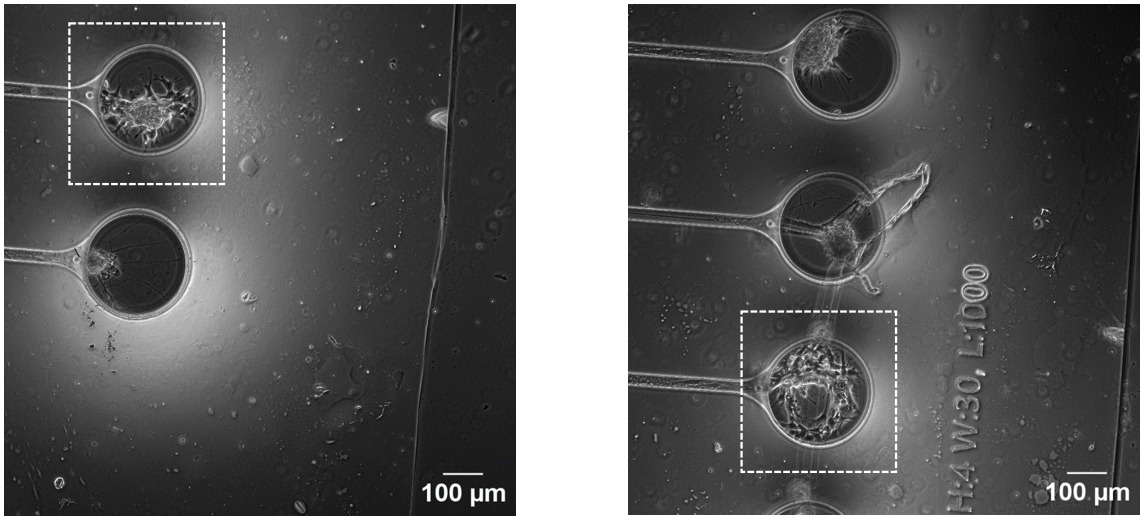

Figure 32: GBM and neurons networks on 10 wt% GelMA at DIV2. The visual representations depict the migration of GBM spheroids within enclosed microstructures filled with 10 wt% GelMA hydrogels.

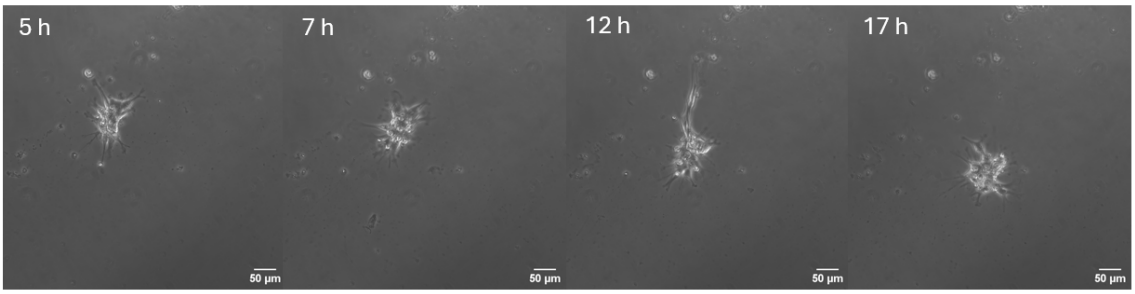

Figure 33: GBM spheroids on 10 wt% GelMA over time. The graphical representation depicts various stages of the growth of a single spheroid overtime on a 10 wt% GelMA scaffold.

The migration of GBM cells over time on substrates with varying stiffness was investigated to assess cancer cell movement from the spheroid body. Different spheroids growing on different scaffolds or in different regions within the same scaffold have been imaged over time. Initial observations indicate minimal cell migration (Figure 32 a) on soft substrates, while cells demonstrate migration from the cancer spheroids on stiffer substrates (Figure 32 b). Additionally, GBM spheroid motility was evaluated by analyzing protrusions extending directly from the spheroid's body starting 5 hours after seeding. Time-lapse imaging (Figure 33) illustrates the dynamic nature of these protrusions, depicting changes in morphology as they extend and retract over time.

4 Discussion

4.1 Mechanical analysis

Rheological and FFM analyses were conducted to evaluate the **mechanical properties** of hydrogels with varying polymer concentrations, aiming to **correlate these properties** with **cell behaviors** such as growth, migration, and proliferation. The focus was on understanding how the **stiffness** and **viscoelasticity** of the hydrogels influence these cellular activities.
Since the cross-linker concentration was kept **constant** across all hydrogel samples, the primary variable affecting the mechanical properties of the gels was the **polymer weight percentage**. Typically, a higher polymer concentration leads to a stiffer hydrogel due to the **increased density** of **polymer chains**, which results in **more crosslinking points** and a higher degree of chain entanglement.

The response of gels to mechanical stress determines whether they exhibit **elastic** or **plastic** behavior. Elastic materials promptly return to their **original shape** when stress is released, while plastic materials undergo **permanent deformation**. Hydrogels can exhibit both elastic and viscous behaviors depending on the degree of polymer chain entanglement and the magnitude of applied stress.
The mechanical properties of hydrogels, as determined by rheological measurements, are governed by two crucial parameters: the **storage modulus** (G') representing **elastic properties**, and **the loss modulus** (G") reflecting the **viscous nature**. At low strain amplitudes, the hydrogel primarily exhibits **elastic behavior**, with G' being greater than G". In this **linear viscoelastic region** (LVR), the mechanical properties remain relatively independent of the applied strain amplitude. Once the strain exceeds a critical value, G" surpasses G', indicating a **transition to viscous behavior** as the material begins to flow and loses its solid-like structure. The tanδ value, which is the ratio of G" to G', captures the relationship between these stress components. The phase angle δ between the applied sinusoidal stress and the material's response is crucial for distinguishing between elastic and viscous regions. In the elastic region, the response is **almost instantaneous** with the phase angle close to 0°, and the material's modulus is dominated by the elastic component. As the strain amplitude increases, the material enters the viscous region, and the phase angle **shifts towards 90°**, signifying a complete out-of-phase stress and response, with the modulus being governed solely by the viscous component, G".

Rheological measurements have demonstrated that an increase in polymer concentration within GelMA-based gels results in a higher storage modulus, leading to enhanced elastic properties and stiffness. This observed phenomenon is attributed to the heightened polymeric chain entanglement and reduced porous structure. Previous research has established that as the overall hydrogel concentration rises for both GelMA and HAMA-based hydrogels, the pore sizes decrease, and this trend may stem from the capacity of hydrogels with lower polymeric content to absorb more water[54]. Furthermore, it has been substantiated that larger pore sizes correspond to heightened gel swelling capabilities [54]. Consequently, for GelMA and HAMA-based gels, an increase in polymer concentration yields scaffold stiffening due to alterations in scaffold structure and morphology. Numerous studies have been undertaken to investigate the combination of GelMA and HAMA hydrogels. In this instance, the hydrogel scaffold is distinguished by the interpenetration of the two polymers and stronger covalent bonds between HAMA and GelMA after photopolymerization, resulting in an increased crosslinking density and stiffening of the hybrid composition compared to the GelMA-only based gel [54]. Furthermore, as outlined in section 1.5.4, the incorporation of HA into scaffolds made from other natural polymers, such as collagen, has a similar effect of enhancing the stiffness of the gels. It has been observed that collagen-based hydrogels containing HA can elevate their Young's modulus to over 1000 Pa, a finding consistent with the conducted analysis. Rheological measurements are reproducible and consistent with the initial assumptions and less susceptible to variations, such as **differences in crosslinking distribution** within the gel mixture and the **stock solution** used to prepare the gel if compared to FFM measurements.

As discussed in section 2.2.3, indeed, FFM employs the **indentation method**, which involves applying a test force to the sample and measuring the resulting indentation depth. For stiffer materials, the force versus indentation curves are **steeper**, indicating that a lower indentation depth is achieved for a given force. Conversely, for softer gel formulations, these curves are **broader**, reflecting a greater indentation depth for the same applied force due to the material's **higher compliance**. Additionally, FFM measurements are influenced by the local composition and stiffness of the sample. In particular, for softer gels, the force versus indentation curves can vary significantly at different points on the same sample, making this measurement method more sensitive to local variations in the gel compared to rheological measurements.

Also the stock solution used for the hydrogel fabrication in this kind of analysis can impact the results. For instance, when preparing a 3% GelMA from a 6.5% stock solution and 5% and 10% gels from a 13% stock solution, approximately 23 μl of polymer is utilized for the 3% GelMA, compared to about 19 μl for the 5% GelMA. Consequently, the marginal difference in the volume of polymer used may lead to a softer gel for the 5% concentration, despite its theoretically higher polymer content.

To address this consideration, the measurements were performed by producing gels within the same stiffness range (e.g., 3% and 5% wt% gels) from the same stock solution. Under consistent conditions, a higher volume of GelMA solution led to a higher Young's modulus, which, however, did not differ significantly from the modulus of the softer gel. It is noteworthy that there is a notable disparity in the quantity of points acquired for the various gel compositions. Specifically, nanoindentation measurements proved to be facile and consistent for the **most rigid** formulation, allowing for the testing of multiple regions from the same sample. Conversely, for the softest concentrations, the acquisition of data points was notably **limited**. This suggests that the softer gels posed greater difficulty in testing, resulting in less reproducible values. In general, the absolute values obtained from the two analyses are not directly comparable due to the differing nature of force application. One case involves shear stress, while the other involves indentation application.

4.2 Cell's surface on different stiffnesses

When placed into scaffolds, cells perceive mechanical cues, such as **stiffness** and **contractility**, which significantly influence their growth [55]. Among the various factors impacted by the substrate, the cell spreading area is particularly crucial, and it has long been recognized as a **key structural property** that influences the cell's internal organization and fate.
Cell adhesion and spreading are facilitated by **actin fibers** within the cytoskeleton, which attach to the extracellular matrix or, in this context, to the hydrogel surface, through focal adhesions, which are large, complex macromolecular assemblies (Figure 34 a) [56][57]. Previous studies have shown that cellular traction forces are crucial for cell adhesion and migration, with these forces being modulated by the elasticity of the surrounding matrix; specifically, **traction forces** increase as substrate stiffness increases [58]. This causes cells to **spread more** extensively on **stiffer substrates** compared to softer ones.
Furthermore, evidence indicates that adhesion site size grows in a stiffness-dependent manner, enabling cells to establish more attachment points on stiffer substrates (Figure 34 b, c), which aids in their spreading across the matrix [55]. This process is also linked to the organization of the actin cytoskeleton, which, on stiffer gels, tends to form stress fibers that terminate at focal adhesion points, thereby increasing the likelihood of cell spreading. Moreover, as detailed in section 4.1, stiffer gels demonstrate reduced porosity. This is attributed to the heightened polymer concentration, resulting in increased crosslinking density and entanglement of polymeric chains. These factors contribute to forming more compact structures, facilitating enhanced cell spreading.

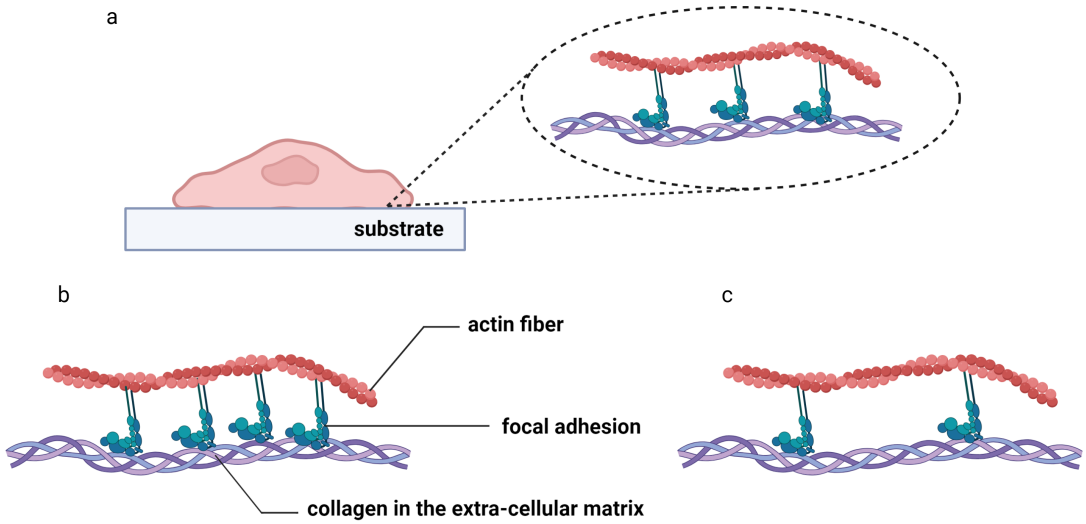

Figure 34: Cell's spreading on different substrates. In the image, is depicted the mechanism through which the cells attach to the substrate and then spread more or less depending on the focal adhesion of the substrates (a). Stiffer substrates promote a more spread-like behavior of the cell between the actin fibers and the collagen polymeric chains present in the extracellular matrix through focal adhesion. This is more pronounced in stiffer substrates compared to softer substrates (c).

As explained in section 3.1, there is a **consistent trend** in the nucleus surface values for the gels. However, this trend is not observed when transitioning to 2D cultures on PDMS microstructures. Therefore, further investigations were required to comprehensively characterize cell behavior on substrates with varying stiffness. Beyond measuring nucleus size, the **total average cell surface** was accessed by computing the **Nestin** and **GFAP** positive regions.
As detailed in section 2.2.5, these markers stain the entire **cytoskeleton**, offering a more accurate evaluation of cells spreading across different hydrogel matrixes. This analysis revealed a progressive increase in cell surface area from the softest GelMA formulations to PDMS and glass, consistently

with the initial assumption, meaning that the increased stiffness of the substrate enhances the spreading of the cell body over the scaffolds. (Figures 2223).

4.3 Axon length and branching on different hydrogels stiffnesses

As discussed in section 1.5.4, hydrogels are well-suited for supporting cell growth due to their mechanical tunability and biocompatibility, including their high water retention capabilities.
During the early stages of development, immature neurons extend axons toward target areas. This initial phase is characterized by the **elongation of axons and dendrites** from the neuronal soma **without branching** . Essentially, it involves the primary protrusions extending further without any additional branching from these primary extensions [59].
Neurite growth is influenced by both chemical and mechanical factors. Beyond chemical signals, variations in stiffness and viscoelasticity play a crucial role in determining the rate and pattern of neurite growth and branching *in vitro*. Moreover, the interplay between these mechanical factors and chemical signals can significantly impact cell behavior and growth rate [59].

Neurons possess growth cones at the tips of their neurites or axons, which function as **sensory compartments** to explore their external microenvironment. These growth cones can detect both **mechanical and chemical signals** from the surrounding matrix . This capability is crucial not only during the early stages of neuronal development and differentiation but also during later stages of terminal differentiation and maturation, as growth cones continue to influence the plasticity of the neuronal network [60]. This is why, especially in the early stages, neurites **may advance and retract** they are actively exploring and moving toward specific targets, guided by regions with suitable stiffness for cell protrusion and spreading. The kinetics of axon outgrowth suggests that a **net force** is necessary for axons to extend or change direction [61]. Two main structural proteins are responsible for axon growth (actin which polymerizes in filaments and tubulin which forms microtubules) and several forces contribute to the forward movement of the axon. **Actin filaments**, which provide **structural support** to the cell, are connected to myosin motor proteins that generate a backward-directed pulling force [61]. Simultaneously, the growth cone exerts a forward-pushing force to promote axon extension. If the force generated by the **growth cone exceeds the opposing contractile force**, the axon will extend overall.

Studies have demonstrated that more compliant substrates result in increased neurite extension and branching compared to stiffer matrices, with compliant substrates having Young's modulus in the range of 100 to 1000 Pa, which spans the bounds of brain tissue stiffness [62]. However, stiffer substrates, around 1000 Pa Young's modulus, have been shown to better support neuronal growth during the first 24 hours *in vitro* with longer neurites observed on stiffer substrates compared to softer ones [59]. Furthermore, a stiffer substrate generally contains more crosslinking points within the hydrogel network, providing a **greater number of attachment sites** for the growth cone to advance. As neurons grow on the gel's backbone structure, this increased availability of attachment points is crucial during the initial hours *in vitro*, as it offers more traction forces for neurites to extend effectively. Another important parameter to consider in this type of analysis is the inclusion of **HAMA** in the gel matrix, alongside GelMA. While comparing 10 wt% GelMA-based hydrogels to 3 wt% GelMA-based gels, it is evident that only the stiffness changes. However, in the case of HAMA + GelMA-based gels, the chemical composition also influences cell growth. It is noteworthy that although stiffer substrates seem to enhance neurite extension in the early stages of neuron growth, this does not unequivocally imply that they universally promote superior neurite development.

After the first 2-3 days *in vitro*, the neuronal network becomes markedly more complex, with neurites and axons not only elongating from the neuron body but also interacting to create more intricate branched networks. Previous studies have demonstrated that **softer substrates** tend to promote a**more branched structure** within the neuronal network [63]. In our case, branching analysis (Figure 28) indicates a considerable **cell-to-cell variability**, where cells do not commence

growth simultaneously, with certain spheroids requiring multiple days of incubation before initiating growth. This variability may account for the decrease in maximum branching number observed for the softest gel concentration at DIV 10. Furthermore, diverse gels with the same concentration but originating from different stock solutions influence neuron growth differentially, contributing to notable variability even for identical gel concentrations. Additionally, the elongation of growing neurites occurs intermittently, with periods of extension interspersed with phases of rest , aligning with the observed results. This highlights that while a softer substrate can expedite neurite branching owing to its greater compliance, a stiffer substrate can still effectively guide neuronal development, albeit over an extended duration.

It is also pertinent to note, as mentioned in section 4.3, that growth cones serve as the primary force driving neuronal growth and branching. Previous research has demonstrated that growth cones can induce significant deformation in gels with a stiffness of up to approximately 300 Pa [64], corresponding to the Young's modulus of 10 wt% GelMA hydrogels. Given that the maximum measured Young's modulus for our gels is 400 Pa, it can be inferred that neurons can effectively grow on all substrates.

4.4 GBM behaviour on different stiffnesses

To investigate how cancer behavior varies with different stiffness levels, analyses were conducted on cancer proliferation, marker expression, and migration.

4.4.1 GBM proliferation ratio

Cancer proliferation was evaluated using **immunohistochemistry**, with hydrogel samples stained for functional markers as outlined in section 2.2.5. Previous studies have demonstrated that Ki67 marker expression increases as one moves from the tumor's outer invasion front towards its core [65]. Specifically, the Ki67-positive fraction was recorded at 39% for core samples (range 4–61%), 26% for rim samples (the outer region of the tumor in contact with surrounding tissues, range 2–45%), and 22% for invasive margin samples (range 4–39%) [65]. The investigation encompassed the examination of resected tumor samples from different regions (such as core, rim, and periphery) of primary glioblastoma multiforme, followed by an assessment using Ki67 immunohistochemistry. Therefore our findings align with observed trends, showing higher proliferation in stiffer gels and similar variability in maximum and minimum values. This variability is attributed to the intrinsic heterogeneity of cells and the variability within tumor tissue as mentioned in section 1.1.1. Like cancer tissue, gels exhibits localized changes in stiffness that influence proliferation rate variability.

Stiffer gels, with their higher proliferation rates, better mimic the tumor core, while softer gels more closely resemble the invasion region of the tumor, particularly the rim/periphery. Previous studies, indeed, have confirmed that tumor core stiffness ranges from 600 Pa to 1.3 kPa, rim tissue stiffness ranges from 300 to 500 Pa, and non-neoplastic tissue measures around 330 Pa (AFM measurements) [66]. Furthermore, although the absolute stiffness values of core and rim regions differ among patients, a consistent core/rim stiffness ratio greater than 1.5 has been observed across all patients [66]. In general, stiffer substrates are known to promote cancer cell proliferation by activating mechanotransduction mechanisms originating in the extracellular matrix. On such substrates, **mechanotransductive and mitogenic** signaling pathways that support cancer proliferation and malignancy are typically activated [67]. One plausible explanation for the role of ECM stiffness in promoting cancer proliferation is the **clustering of surface receptors** (e.g., integrins), which enhances their **signaling activity** and consequently activates various pathways, such as the **ERK pathway** and **Rho GTPase pathway**. These pathways prompt cells to enter a proliferative state and further stiffen their cytoskeleton [67].

Despite these initial findings, there is still much to be understood about how Ki67 expression varies with substrate stiffness. Other studies have reported increased Ki67 expression in the tu-

mor's invasion region [68], which is softer compared to the tumor core. This variation in behavior could be attributed to factors such as **patient variability** or the **specific region from which the tumor was resected**. As a preliminary test, the effectiveness of the 3D *in vitro* model using hydrogels was assessed by comparing the proliferation ratios obtained from these hydrogels to data from human brain tumor slices. Brain slices are typically noisier than hydrogel cancer samples, requiring high-resolution imaging to eliminate background noise that remains after PBS washes during the staining procedure 2.2.5. Initial results still show variability in proliferation within the brain slices 1.1.1. The variability is more accurately reflected by gel samples than 2D cultures on PDMS. This is attributed to the 3D structures and locally varying mechanical properties of hydrogel scaffolds, enabling a more faithful mimicry of the intricate nature of the extracellular brain matrix and intratumoral heterogeneity. Consequently, the hydrogel model effectively emulates in vivo tumor behavior.

4.4.2 GBM markers expression: Nestin and GFAP

To complete the characterization of cancer on different GelMA scaffolds and assess their malignancy and infiltration, the overall percentage of cells positive for Nestin and GFAP was analyzed. As discussed in section 2.2.5, Nestin expression is linked to tumor malignancy and proliferation [69], while GFAP expression is a key indicator of tumor cell differentiation.
In neuroepithelial tumors, Nestin expression is elevated in malignant gliomas compared to benign gliomas. Additionally, increased Nestin expression is linked to **higher-grade gliomas and poorer patient survival rates** [70] [7]. The analysis aimed to explore how Nestin expression levels vary with different gel stiffnesses to determine if stiffer substrates lead to increased expression of this marker, potentially contributing to a more aggressive form of GBM development. Previous studies on *in vivo* brain slices have examined the stemness of GBM cell populations across different tumor regions through Nestin immunohistochemistry. These studies have shown that Nestin expression is reduced in the invasive areas of the tumor, which are typically associated with a softer matrix and lower Young's modulus. Specifically, it has been demonstrated that the GBM **invasive margin** has **lower levels of Nestin** expression compared to the tumor core, with the core exhibiting about 80% Nestin positivity and the invasive region showing only 23% Nestin positivity [65].
The results of our analysis indicate that there is a higher average percentage of Nestin-positive cells in stiffer gels, which is consistent with the findings mentioned. However, it is important to note that direct comparison between the absolute values from *in vivo* brain slices studies and the results obtained for the gels may not be appropriate, as the marker expression is specific to each patient. Nevertheless, these preliminary analyses provide further support for the notion that Nestin expression is likely to be higher in the case of stiffer substrates.

Turning to GFAP expression, as discussed in section 2.2.5, this protein serves as a marker for astrocyte maturation and is utilized to assess the glial origin of the tumor [7].
According to previous studies, GFAP is most pronounced in the tumor core, with reduced GFAP levels observed in invasive regions [68]. In our study, although the average percentage of GFAP-positive cells is slightly higher on stiffer substrates, the difference is minimal, less than 1%. However, other research has reached different conclusions regarding GFAP expression.

Immunohistochemistry scores for high-grade gliomas **have not revealed significant differences in GFAP expression** and GFAP levels have not been correlated with tumor survival prognosis, suggesting that GFAP may not be as effective as Nestin in assessing tumor aggressiveness and targeting efficiency [71]. The findings for this analysis indicate that GFAP serves as a marker for differentiated tumor cells, whereas Nestin expression is more closely linked to tumor proliferation and aggressiveness. However, further investigations are required to thoroughly evaluate the dependency of the marker expression across different patients.

4.4.3 Neurons and GBM network

Understanding cancer cell behavior involves also studying how their movement is influenced by interactions with neuronal networks and how efficiently they can remodel these networks. Evidence indicates a **bidirectional relationship between neurons and GBM cells**. Neuronal activity, which affects precursor regulation, electrochemical signaling, and neuronal secretion, has a significant impact on gliomas. Numerous studies highlight the importance of the tumor microenvironment (TME) in glioma progression. The TME includes non-glioma brain cells such as glial cells, immune cells, and neurons that gliomas co-opt to create a supportive environment for tumor growth. This is reflected in the fact that gliomas **rarely metastasize outside the CNS**, suggesting that neurons play a crucial role in driving cancer progression, migration, and extracellular matrix remodeling.

GBM cells released near neuronal networks exhibit **higher speeds** compared to those not near such networks. This is supported by data comparing the velocity of spheroids and single cells near neuronal networks to those in random regions of the bulk gels. These findings align with previous research demonstrating that neuronal activity enhances glioma cell initiation, growth, and invasion [72]. The migration of neural progenitors and stem cells is impacted by the electric currents generated by local field potentials [73]. Specifically, direct-current electric fields, through **galvanotaxis**, influence cell migration by inducing alterations in intracellular calcium concentrations and ion channel activities [74]. These currents have the potential to cause the **redistribution of charged molecules** such as ions and proteins on the cell's membrane, as well as the **activation of ion channels**. This cumulative effect results in the polarization of the cell itself and an increase in its motility [74]. This might elucidate the heightened speed and motility of glioma cells toward neurites.

Another important factor in assessing cancer cell aggression and invasion is the protrusions extending from the cell body. Stiffer substrates typically encourage **faster and more aggressive cancer growth** right after spheroids are seeded into gels. However, accurately measuring these protrusions is difficult because they frequently elongate and retract in a dynamic manner similar to neuronal behavior, as discussed in section 4.3. This behavior is consistent with previous research demonstrating that spheroids extend multiple highly dynamic protrusions that rapidly cycle between elongation and retraction [75].
The formation of invasive protrusions is especially important in early tumorigenesis [75]. These protrusions enable tumors to adhere and migrate on their substrate, facilitating further movement through mechanical force. Research also highlights the crucial role of actin in protrusion formation, with actin polymerization and depolymerization driving the extension and retraction of these protrusions. Another interesting consideration when comparing gel stiffnesses is that stiffer substrates seem to promote greater migration of single cells from spheroids at the early stages of cancer growth. One potential explanation is that the mechanical characteristics of the substrate directly influence the cell cycle in particular during **cytokinesis**, the phase in which the cell membrane constricts to divide into two daughter cells. Specifically, when a cell encounters greater frictional forces on a rigid substrate, it may experience **cellular asymmetries and distortion** as it attempts division. Consequently, this triggers the activation of compensatory contractile forces, ultimately **increasing cell motility** [67].

4.5 Conclusion

The development of a 3D *in vitro* platform for investigating the growth of neurons and glioblastoma under various substrate stiffness conditions has yielded valuable insights into the interactions and behaviors of these cell types. The findings underscore the significant roles played by both the mechanical properties of the extracellular matrix and biological signals in influencing cell response, proliferation, migration, and growth.

The tested range of stiffnesses has revealed that both stiffer and softer gels are effective in promoting neuronal growth with the stiffer gels supporting better neurite elongation during the initial hours *in vitro*, while more compliant substrates encouraged branching over subsequent days. However, the analysis is substantially influenced by cell variability.
Additionally, heightened migration, proliferation, and expression of tumor malignancy markers were observed on stiffer substrates, indicating an enhancement of the ERK pathway and Rho GTPase pathway, which are responsible for cancer proliferation and migration. Initial comparisons with brain slice analysis results suggest that the variability in proliferation rates for cells cultured on hydrogel scaffolds closely resembles that of brain slices, as opposed to the low variability observed in 2D culture on PDMS, meaning that 3D hydrogel models offer a more accurate representation of the mechanical properties variability found within the human brain, mimicking better the in vivo condition. The motility of GBM cells has been evaluated in relation to their proximity to neuronal networks and stiffness of the substrates. The findings confirm that neuronal electrical activity significantly influences the motility of cancer cells. Specifically, the average velocity of the cells is notably higher in close proximity to neurites. Migration in relation to the stiffness of the substrate is challenging to compute due to the spheroid's protrusion elongating and retracting over time. Conversely, when considering cell migration from the spheroid's body, it has been observed that stiffer substrates appear to facilitate improved migration over time.

Moving forward, refinement of the compartmentalization of co-culture systems in PDMS microstructures and improvement of the gel seeding procedure to prevent unwanted cell growth outside designated areas are recommended. Furthermore, additional exploration of different compositions of hyaluronic acid for enhancing matrix stiffness to both explore a wider range of stiffness and better mimic the complexity of brain ECM should be pursued in order to characterize how the chemical composition can affect cancer and neuron growth. Investigating cell phenotypes through single-cell cultures could provide more detailed insights, with the analysis focusing on single-cell analysis instead of an average analysis made on cancer growing as 3D spheroids. Overall, the 3D spheroid experiments warrant continued investigation, as they offer an accurate representation of cell behavior and should continue to be explored to gain a deeper understanding of cell-to-cell interactions and the real cellular environment.

References

[1] S. S. Herbert B. Newton, "Overview of Brain Tumor Epidemiology and Histopathology," *Handbook of Brain Tumor Chemotherapy, Molecular Therapeutics, and Immunotherapy (Second Edition)*, vol. Chapter 1, pp. 3–20, 2018.

[2] J. R. D. Pearson and T. Regad, "Targeting cellular pathways in glioblastoma multiforme," *Signal Transduction and Targeted Therapy*, vol. 2, p. 17040, September 2017.

[3] F. Hanif, K. Muzaffar, K. Perveen, S. M. Malhi, and S. U. Simjee, "Glioblastoma Multiforme: A Review of its Epidemiology and Pathogenesis through Clinical Presentation and Treatment," *Asian Pacific Journal of Cancer Prevention*, vol. 18, no. 1, pp. 3–9, January 2017.

[4] J. P. Thakkar, T. A. Dolecek, C. Horbinski, Q. T. Ostrom, D. D. Lightner, J. S. Barnholtz-Sloan, and J. L. Villano, "Epidemiologic and molecular prognostic review of glioblastoma," *Cancer Epidemiology, Biomarkers Prevention*, vol. 23, no. 10, pp. 1985–1996, October 2014, epub 2014 Jul 22.

[5] Q. T. Ostrom, N. Patil, G. Cioffi, K. Waite, C. Kruchko, and J. S. Barnholtz-Sloan, "CBTRUS Statistical Report: Primary Brain and Other Central Nervous System Tumors Diagnosed in the United States in 2013-2017," *Neuro-oncology*, vol. 22, no. 12 Suppl 2, pp. iv1–iv96, October 2020.

[6] W. Wu, J. L. Klockow, M. Zhang, F. Lafortune, E. Chang, L. Jin, Y. Wu, and H. E. Daldrup-Link, "Glioblastoma multiforme (GBM): An overview of current therapies and mechanisms of resistance," *Pharmacological Research*, vol. 171, p. 105780, September 2021.

[7] A. Bradshaw, A. Wickremsekera, S. T. Tan, L. Peng, P. F. Davis, and T. Itinteang, "Cancer Stem Cell Hierarchy in Glioblastoma Multiforme," *Frontiers in Surgery*, vol. 3, p. 21, April 2016, eCollection 2016.

[8] F. Ah-Pine, M. Khettab, Y. Bedoui, Y. Slama, M. Daniel, B. Doray, and P. Gasque, "On the Origin and Development of Glioblastoma: Multifaceted Role of Perivascular Mesenchymal Stromal Cells," *Acta Neuropathologica Communications*, vol. 11, no. 1, p. 104, 2023.

[9] M. L. Uribe, I. Marrocco, and Y. Yarden, "EGFR in Cancer: Signaling Mechanisms, Drugs, and Acquired Resistance," *Cancers (Basel)*, vol. 13, no. 11, p. 2748, June 2021, ePublish.

[10] Y. Zhang, C. Dube, M. G. Jr, N. Cruickshanks, B. Wang, M. Coughlan, Y. Yang, I. Setiady, C. Deveau, K. Saoud, C. Grello, M. Oxford, F. Yuan, and R. Abounader, "The p53 Pathway in Glioblastoma," *Cancers*, vol. 10, no. 9, p. 297, September 2018.

[11] S. W. Choi, Y. Lee, K. Shin, H. Koo, D. Kim, J. K. Sa, H. J. Cho, H.-M. Shin, S. J. Lee, H. Kim, S. Chung, J. Shin, C. Lee, and D.-H. Nam, "Mutation-specific non-canonical pathway of PTEN as a distinct therapeutic target for glioblastoma," *Cell Death Disease*, vol. 12, no. 4, p. 374, April 2021.

[12] R. Gómez-Oliva, S. Domínguez-García, L. Carrascal, J. Abalos-Martínez, R. Pardillo-Díaz, C. Verástegui, C. Castro, P. Nunez-Abades, and N. Geribaldi-Doldán, "Evolution of Experimental Models in the Study of Glioblastoma: Toward Finding Efficient Treatments," *Frontiers in Oncology*, vol. 10, p. 614295, January 2020.

[13] N. Yadav and B. W. Purow, "Understanding current experimental models of glioblastoma-brain microenvironment interactions," *Journal of Neuro-Oncology*, vol. 166, no. 2, pp. 213–229, January 2024, ePub.

[14] Q. Shu, K. K. Wong, J. M. Su, A. M. Adesina, L. T. Yu, Y. T. M. Tsang, B. C. Antalffy, P. Baxter, L. Perlaky, J. Yang, R. C. Dauser, M. Chintagumpala, S. M. Blaney, C. C. Lau, and X.-N. Li, "Direct Orthotopic Transplantation of Fresh Surgical Specimen Preserves CD133+

Tumor Cells in Clinically Relevant Mouse Models of Medulloblastoma and Glioma," *Stem Cells*, vol. 26, no. 6, pp. 1414–1424, June 2008.

[15] D. W. Parsons, S. Jones, X. Zhang, J. C.-H. Lin, R. J. Leary, P. Angenendt, P. Mankoo, H. Carter, I.-M. Siu, G. L. Gallia, A. Olivi, R. McLendon, B. A. Rasheed, S. Keir, T. Nikolskaya, Y. Nikolsky, D. A. Busam, H. Tekleab, L. A. D. Jr, J. Hartigan, D. R. Smith, R. L. Strausberg, S. K. N. Marie, S. M. O. Shinjo, H. Yan, G. J. Riggins, D. D. Bigner, R. Karchin, N. Papadopoulos, G. Parmigiani, B. Vogelstein, V. E. Velculescu, and K. W. Kinzler, "An integrated genomic analysis of human glioblastoma multiforme," *Science*, vol. 321, no. 5897, pp. 1807–1812, September 2008.

[16] N. Yadav and B. W. Purow, "Understanding current experimental models of glioblastoma-brain microenvironment interactions," *Journal of Neuro-Oncology*, vol. 166, no. 2, pp. 213–229, January 2024. [Online]. Available: https://doi.org/10.1007/s11060-023-04536-8

[17] A. Saraswathibhatla, D. Indana, and O. Chaudhuri, "Cell-extracellular matrix mechanotransduction in 3D," *Nature Reviews Molecular Cell Biology*, vol. 24, no. 7, pp. 495–516, July 2023.

[18] M. Kapałczyńska, T. Kolenda, W. Przybyła, M. Zajączkowska, A. Teresiak, V. Filas, M. Ibbs, R. Bliźniak, Łukasz Łuczewski, and K. Lamperska, "2D and 3D cell cultures - a comparison of different types of cancer cell cultures," *Archives of Medical Science*, vol. 14, no. 4, pp. 910–919, June 2018.

[19] D. Lv, Z. Hu, L. Lu, H. Lu, and X. Xu, "Three-dimensional cell culture: A powerful tool in tumor research and drug discovery," *Oncology Letters*, vol. 14, no. 6, pp. 6999–7010, 2017.

[20] N. Chaicharoenaudomrung, P. Kunhorm, and P. Noisa, "Three-dimensional cell culture systems as an in vitro platform for cancer and stem cell modeling," *World Journal of Stem Cells*, vol. 11, no. 12, pp. 1065–1083, December 2019.

[21] S. S. Rao, J. Dejesus, A. R. Short, J. J. Otero, A. Sarkar, and J. O. Winter, "Glioblastoma behaviors in three-dimensional collagen-hyaluronan composite hydrogels," *ACS Applied Materials Interfaces*, vol. 5, no. 19, pp. 9276–9284, 2013, published online 6 September 2013.

[22] T.-C. Ho, C.-C. Chang, H.-P. Chan, T.-W. Chung, C.-W. Shu, K.-P. Chuang, T.-H. Duh, M.-H. Yang, and Y.-C. Tyan, "Hydrogels: Properties and Applications in Biomedicine," *Molecules*, vol. 27, no. 9, p. 2902, May 2022.

[23] B. S. Kaith, A. Singh, A. K. Sharma, and D. Sud, "Hydrogels: Synthesis, Classification, Properties and Potential Applications—A Brief Review," *Journal of Polymers and the Environment*, vol. 29, pp. 3827–3841, 2021.

[24] S. Bashir, M. Hina, J. Iqbal, A. H. Rajpar, M. A. Mujtaba, N. A. Alghamdi, S. Wageh, K. Ramesh, and S. Ramesh, "Fundamental Concepts of Hydrogels: Synthesis, Properties, and Their Applications," *Polymers*, vol. 12, no. 11, p. 2702, November 2020.

[25] T.-L. Sun, T. Kurokawa, S. Kuroda, A. B. Ihsan, T. Akasaki, K. Sato, M. A. Haque, T. Nakajima, and J.-P. Gong, "Physical hydrogels composed of polyampholytes demonstrate high toughness and viscoelasticity," *Nature Materials*, vol. 12, no. 10, pp. 932–937, October 2013.

[26] X. Hu, M. Vatankhah-Varnoosfaderani, J. Zhou, Q. Li, and S. S. Sheiko, "Weak Hydrogen Bonding Enables Hard, Strong, Tough, and Elastic Hydrogels," *Advanced Materials*, vol. 27, no. 43, pp. 7028–7033, October 2015.

[27] J. Maitra and V. K. Shukla, "Cross-linking in Hydrogels - A Review," *American Journal of Polymer Science*, vol. 4, no. 2, pp. 25–31, 2014.

[28] T. Saleh, "Polymer Science and Polymerization Methods Toward Hybrid Materials," pp. 59–103, 01 2021.

[29] M. Khoonkari, D. Liang, M. Kamperman, F. A. E. Kruyt, and P. van Rijn, "Physics of Brain Cancer: Multiscale Alterations of Glioblastoma Cells under Extracellular Matrix Stiffening," *Pharmaceutics*, vol. 14, no. 5, p. 1031, May 10 2022.

[30] A. Wade, A. E. Robinson, J. R. Engler, C. Petritsch, C. D. James, and J. J. Phillips, "Proteoglycans and their roles in brain cancer," *FEBS Journal*, vol. 280, no. 10, pp. 2399–2417, May 2013.

[31] M. Wu, K. Cronin, and J. S. Crane, "Biochemistry, Collagen Synthesis," 2023, last Update: September 4, 2023.

[32] B. Yue, "Biology of the Extracellular Matrix: An Overview," *Journal of Glaucoma*, vol. 23, no. 8 Suppl 1, pp. S20–S23, October-November 2014.

[33] J. Berlanga-Acosta, J. Gavilondo-Cowley, P. López-Saura, T. González-López, M. D. Castro-Santana, E. López-Mola, G. Guillén-Nieto, and L. Herrera-Martínez, "Epidermal growth factor in clinical practice - a review of its biological actions, clinical indications and safety implications," *International Wound Journal*, vol. 6, no. 5, pp. 331–346, Oct 2009.

[34] Q. Zheng, H. Liu, W. Yu, Y. Dong, L. Zhou, W. Deng, and F. Hua, "Mechanical properties of the brain: Focus on the essential role of Piezo1-mediated mechanotransduction in the CNS," *Brain and Behavior*, vol. 13, no. 9, p. e3136, September 2023.

[35] A. Procès, M. Luciano, Y. Kalukula, L. Ris, and S. Gabriele, "Multiscale Mechanobiology in Brain Physiology and Diseases," Ph.D. dissertation, March 2022.

[36] C. F. Guimarães, L. Gasperini, A. P. Marques, and R. L. Reis, "The stiffness of living tissues and its implications for tissue engineering," *Nature Reviews Materials*, vol. 5, pp. 351–370, February 2020.

[37] A. Soles, A. Selimovic, K. Sbrocco, F. Ghannoum, K. Hamel, E. L. Moncada, S. Gilliat, and M. Cvetanovic, "Extracellular Matrix Regulation in Physiology and in Brain Disease," *International Journal of Molecular Sciences*, vol. 24, no. 8, p. 7049, April 11 2023.

[38] M. Khoonkari, D. Liang, M. Kamperman, F. A. E. Kruyt, and P. van Rijn, "Physics of Brain Cancer: Multiscale Alterations of Glioblastoma Cells under Extracellular Matrix Stiffening," *Pharmaceutics*, vol. 14, no. 5, p. 1031, 2022.

[39] J. Huang, L. Zhang, D. Wan, L. Zhou, S. Zheng, S. Lin, and Y. Qiao, "Extracellular matrix and its therapeutic potential for cancer treatment," *Signal Transduction and Targeted Therapy*, vol. 6, no. 1, p. 153, 2021. [Online]. Available: https://doi.org/10.1038/s41392-021-00544-0

[40] T. Yan, X. Chen, H. Zhan, P. Yao, N. Wang, H. Yang, C. Zhang, K. Wang, H. Hu, J. Li, J. Sun, Y. Dong, E. Lu, Z. Zheng, R. Zhang, X. Wang, J. Ma, M. Gao, J. Ye, X. Wang, L. Teng, H. Liu, and S. Zhao, "Interfering with hyaluronic acid metabolism suppresses glioma cell proliferation by regulating autophagy," vol. 12, no. 5, 2021, p. 486.

[41] K. J. Wolf and S. Kumar, "Hyaluronic Acid: Incorporating the Bio into the Material," vol. 5, no. 8, August 2019, pp. 3753–3765.

[42] J. A. Burdick and G. D. Prestwich, "Hyaluronic acid hydrogels for biomedical applications," *Advanced Materials*, vol. 23, no. 12, pp. H41–56, March 2011, review article discussing the development and applications of hyaluronic acid-based hydrogels in biomedicine.

[43] Z. Luo, Y. Wang, Y. Xu, J. Wang, and Y. Yu, "Modification and crosslinking strategies for hyaluronic acid-based hydrogel biomaterials," *Smart Medicine*, 2023.

[44] M. Sun, X. Sun, Z. Wang, S. Guo, G. Yu, and H. Yang, "Synthesis and Properties of Gelatin Methacryloyl (GelMA) Hydrogels and Their Recent Applications in Load-Bearing Tissue," *Polymers*, vol. 10, no. 11, p. 1290, November 2018, review article on Gelatin Methacryloyl

(GelMA) hydrogels, covering synthesis methods, properties, characterization techniques, and applications in load-bearing tissues such as bone and cartilage.

[45] S. Sharifi, H. Sharifi, A. Akbari, and J. Chodosh, "Systematic optimization of visible light-induced crosslinking conditions of gelatin methacryloyl (GelMA)," *Scientific Reports*, vol. 11, no. 1, p. 23276, 2021.

[46] M. Li, L. Liu, and T. Zambelli, "FluidFM for Single-Cell Biophysics," *Journal of Biophysics*, vol. 2021, no. 1, pp. 1–10, 2021.

[47] S. Irgen-Gioro, S. Yoshida, V. Walling, and S. Chong, "Fixation can change the appearance of phase separation in living cells," *eLife*, vol. 11, p. e79903, 2022, pMID: 36444977, PMCID: PMC9817179. [Online]. Available: https://doi.org/10.7554/eLife.79903

[48] E. A. Hoffman, B. L. Frey, L. M. Smith, and D. T. Auble, "Formaldehyde crosslinking: a tool for the study of chromatin complexes," *Journal of Biological Chemistry*, vol. 290, no. 44, pp. 26 404–26 411, 2015. [Online]. Available: https://doi.org/10.1074/jbc.R115.651679

[49] C. Oliver and M. C. Jamur, "Immunocytochemical methods and protocols," *Methods in Molecular Biology*, vol. 588, pp. iv–v, 2010, published: 23 December 2009.

[50] X. Sun and P. D. Kaufman, "Ki-67: more than a proliferation marker," *Chromosoma*, vol. 127, no. 2, pp. 175–186, 2018, review.

[51] A. Bernal and L. Arranz, "Nestin-expressing progenitor cells: function, identity and therapeutic implications," *Cellular and Molecular Life Sciences*, vol. 75, no. 12, pp. 2177–2195, June 2018.

[52] B. M. Chung, J. D. Rotty, and P. A. Coulombe, "Networking galore: intermediate filaments and cell migration." *Current opinion in cell biology*, vol. 25 5, pp. 600–12, 2013.

[53] A. Ganne, M. Balasubramaniam, W. S. T. Griffin, R. J. Shmookler Reis, and S. Ayyadevara, "Glial Fibrillary Acidic Protein: A Biomarker and Drug Target for Alzheimer's Disease," *Pharmaceutics*, vol. 14, no. 7, p. 1354, 2022, published online 2022 Jun 26.

[54] B. Velasco-Rodriguez, T. Diaz-Vidal, L. C. Rosales-Rivera, C. A. García-González, C. Alvarez-Lorenzo, A. Al-Modlej, V. Domínguez-Arca, G. Prieto, S. Barbosa, J. F. A. Soltero Martínez, and P. Taboada, "Hybrid Methacrylated Gelatin and Hyaluronic Acid Hydrogel Scaffolds. Preparation and Systematic Characterization for Prospective Tissue Engineering Applications," *International Journal of Molecular Sciences*, vol. 22, no. 13, p. 6758, 2021.

[55] B. Yi, Q. Xu, and W. Liu, "An overview of substrate stiffness guided cellular response and its applications in tissue regeneration," *Bioactive Materials*, vol. 15, pp. 82–102, 2021.

[56] N. Nisenholz, K. Rajendran, Q. Dang, H. Chen, R. Kemkemer, R. Krishnan, and A. Zemel, "Active mechanics and dynamics of cell spreading on elastic substrates," *Soft Matter*, vol. 10, pp. 7234–7246, 2014.

[57] K. Legerstee and A. B. Houtsmuller, "A Layered View on Focal Adhesions," *Biology (Basel)*, vol. 10, no. 11, p. 1189, 2021.

[58] J. P. Califano and C. A. Reinhart-King, "Substrate Stiffness and Cell Area Predict Cellular Traction Stresses in Single Cells and Cells in Contact," *Cellular and Molecular Bioengineering*, vol. 3, no. 1, pp. 68–75, 2010.

[59] D. E. Koser, A. J. Thompson, S. Foster, A. Dwivedy, E. K. Pillai, G. K. Sheridan, H. Svoboda, M. P. Viana, L. da Fontoura Costa, J. Guck, C. E. Holt, and K. Franze, "Mechanosensing is critical for axon growth in the developing brain," *Nature Neuroscience*, vol. 19, no. 12, pp. 1592–1598, December 2016.

[60] M. Chighizola, T. Dini, C. Lenardi, P. Milani, A. Podestà, and C. Schulte, "Mechanotransduction in neuronal cell development and functioning," *Biophysical Reviews*, vol. 11, no. 5, pp. 701–720, 2019.

[61] V. Raffa, "Force: A messenger of axon outgrowth," *Seminars in Cell Developmental Biology*, vol. 140, pp. 3–12, 2023.

[62] R. Chapla, R. R. Katz, and J. L. West, "Neurogenic Cell Behavior in 3D Culture Enhanced Within a Highly Compliant Synthetic Hydrogel Platform Formed via Competitive Crosslinking," *Cellular and Molecular Bioengineering*, vol. 17, no. 1, pp. 35–48, February 2024.

[63] L. A. Flanagan, Y.-E. Ju, B. Marg, M. Osterfield, and P. A. Janmey, "Neurite branching on deformable substrates," *Neuroreport*, vol. 13, no. 18, pp. 2411–2415, 2002.

[64] K. Franze, J. Gerdelmann, M. Weick, T. Betz, S. Pawlizak, M. Lakadamyali, J. Bayer, K. Rillich, M. Gögler, Y.-B. Lu, A. Reichenbach, P. Janmey, and J. Käs, "Neurite branch retraction is caused by a threshold-dependent mechanical impact," *Biophysical Journal*, vol. 97, no. 7, pp. 1883–1890, 2009.

[65] S. J. Smith, M. Diksin, S. Chhaya, S. Sairam, M. A. Estevez-Cebrero, and R. Rahman, "The Invasive Region of Glioblastoma Defined by 5ALA Guided Surgery Has an Altered Cancer Stem Cell Marker Profile Compared to Central Tumour," *International Journal of Molecular Sciences*, vol. 18, no. 11, p. 2452, 2017.

[66] B. J. Mahaffey, Z. P. Fowler, Z. Lung, V. Dang, H. Lee, A. M. Johnson, M. A. Munoz, D. A. Goodin, H. B. Frieboes, B. J. Williams, and J. Chen, "The prognostic effect of mechanical, ultrastructural, and ECM signatures in glioblastoma core and rim," *APL Bioengineering*, vol. 8, no. 3, p. 036101, 2024.

[67] T. A. Ulrich, E. M. de Juan Pardo, and S. Kumar, "The mechanical rigidity of the extracellular matrix regulates the structure, motility, and proliferation of glioma cells," *Cancer research*, vol. 69, no. 10, pp. 4167–4174, 2009.

[68] A. Fayzullin, C. J. Sandberg, M. Spreadbury, B. M. Saberniak, Z. Grieg, E. Skaga, I. A. Langmoen, and E. O. Vik-Mo, "Phenotypic and Expressional Heterogeneity in the Invasive Glioma Cells," *Vilhelm Magnus Laboratory for Neurosurgical Research, Institute for Surgical Research, Oslo University Hospital, Oslo, Norway*, 2024, department of Neurosurgery, Oslo University Hospital, Oslo, Norway.

[69] J. Neradil and R. Veselska, "Nestin as a marker of cancer stem cells," *Cancer Science*, vol. 106, no. 7, pp. 803–811, 2015, review.

[70] D. Schiffer, A. Manazza, and I. Tamagno, "Nestin expression in neuroepithelial tumors," *Neuroscience Letters*, vol. 400, no. 1-2, pp. 80–85, 2006.

[71] H. Arai, H. Ikota, K. ichi Sugawara, S. Nobusawa, J. Hirato, and Y. Nakazato, "Nestin expression in brain tumors: its utility for pathological diagnosis and correlation with the prognosis of high-grade gliomas," *Brain Tumor Pathology*, vol. 29, no. 3, pp. 160–167, 2012.

[72] X. Guo, W. Qiu, C. Wang, Y. Qi, B. Li, S. Wang, R. Zhao, B. Cheng, X. Han, H. Du, Z. Gao, Z. Pan, S. Zhao, G. Li, and H. Xue, "Neuronal Activity Promotes Glioma Progression by Inducing Proneural-to-Mesenchymal Transition in Glioma Stem Cells," *Cancer Research*, vol. 84, no. 3, pp. 372–387, Feb. 2024.

[73] T. Hua, H. Shi, M. Zhu, C. Chen, Y. Su, S. Wen, X. Zhang, J. Chen, Q. Huang, and H. Wang, "Glioma-neuronal interactions in tumor progression: Mechanism, therapeutic strategies and perspectives (Review)," *International Journal of Oncology*, vol. 61, no. 3, p. 104, 2022.

[74] D. B. Mair, H. M. Ames, and R. Li, "Mechanisms of invasion and motility of high-grade gliomas in the brain," *Molecular Biology of the Cell*, vol. 29, no. 21, pp. 2509–2601, 2018. [Online]. Available: https://doi.org/10.1091/mbc.E18-02-0123

[75] D. Caballero, V. Brancato, A. C. Lima, C. M. Abreu, N. M. Neves, V. M. Correlo, J. M. Oliveira, R. L. Reis, and S. C. Kundu, "Tumor-Associated Protrusion Fluctuations as a Signature of Cancer Invasiveness," *Advanced Biology*, vol. 5, no. 9, p. e2101019, September 2021.

Supplementary Tables

Table 11: Ordinary one-way ANOVA test results for the FFM results. Summary of the test and p-value statistics of the ANOVA test and Tukey's multiple comparisons test for the relative increase in Young modulus with polymer wt% in the gels.

Ordinary One-way ANOVA Test						
P value	<0.0001					
P value summary	****					
F	3156.39					
R squared	0.94					
Tukey's multiple comparisons test						
Comparison	*Mean rank diff.*	*95% C.I.*	*Adjusted P*	*Summary*	*N1*	*N2*
10 wt% vs. 3 wt%	-1815.97	-1906.7937, -1725.1468	<0.0001	****	126	9
10 wt% vs. 5 wt%	-1786.21	-1848.2551, -1724.1666	<0.0001	****	126	21
3 wt% vs. 5 wt%	29.75	-75.1145, 134.6333	0.78	ns	9	21

Table 12: Kruskal-Wallis test results for the cell surface measurements. Test and p-value statistics of the Kruskal-Wallis and post-hoc Pairwise Mann-Whitney U test.

Kruskal-Wallis test				
P value	<0.0001			
Exact or approximate P value?	Approximate			
P value summary	****			
Kruskal-Wallis statistic	152.48			
Pairwise Mann-Whitney U test results				
Comparison	*Adjusted P Value*	*Summary*	*N1*	*N2*
0.03 kPa vs. 0.13 kPa	<0.0001	****	381	385
0.03 kPa vs. 1.3 kPa	<0.0001	****	381	230
0.03 kPa vs. 2000 kPa	<0.0001	****	381	80
0.13 kPa vs. 1.3 kPa	<0.0001	****	385	230
0.13 kPa vs. 2000 kPa	>0.9999	ns	385	80
1.3 kPa vs. 2000 kPa	<0.0001	****	230	80

Table 13: Kruskal-Wallis test results for the proliferation ratio data. Test and p-value statistics of the Kruskal-Wallis and post-hoc Pairwise Mann-Whitney U test.

Kruskal-Wallis test				
P value	<0.0001			
Exact or approximate P value?	Approximate			
P value summary	****			
Kruskal-Wallis statistic	21.10			
Pairwise Mann-Whitney U test results				
Comparison	*Adjusted P Value*	*Summary*	*N1*	*N2*
0.03 kPa vs. 1.3 kPa	0.36	ns	24	20
0.03 kPa vs. 1000 kPa	0.91	ns	37	15
0.03 kPa vs. Brain slices	0.005	**	24	21
1.3 kPa vs. 1000 kPa	0.03	*	20	15
1.3 kPa vs. Brain slices	>0.9999	ns	20	21
2000 kPa vs. Brain slices	0.00031	***	15	21

Table 14: Kruskal-Wallis test results for the Nestin+ cell surface . Test and p-value statistics of the Kruskal-Wallis and post-hoc Pairwise Mann-Whitney U test.

Kruskal-Wallis test				
P value	0.008			
Exact or approximate P value?	Approximate			
P value summary	****			
Kruskal-Wallis statistic	9.6			
Pairwise Mann-Whitney U test results				
Comparison	*Adjusted P Value*	*Summary*	*N1*	*N2*
0.03 kPa vs. 1.3 kPa	0.002	**	25	18
0.03 kPa vs. 1000 kPa	>0.9999	ns	25	17
1.3 kPa vs. 1000 kPa	0.37	ns	18	17

Table 15: Ordinary one-way ANOVA test for Nestin+ cells percentage. Summary of the test and p-value statistics of the ANOVA test and Tukey's multiple comparisons test.

Ordinary One-way ANOVA Test						
P value	<0.0001					
P value summary	****					
F	15.17					
R squared	0.34					
Tukey's multiple comparisons test						
Comparison	*Mean rank diff.*	*95% C.I.*	*Adjusted P*	*Summary*	*N1*	*N2*
0.03 kPa vs. 1.3 kPa	6.23	-1.41, 13.88	0.13	ns	25	18
0.03 kPa vs. 1000 kPa%	-12.55	-20.34, -4.77	0.0008	***	25	17
1.3 kPa vs. 1000 kPa	-18.79	-27.16, -10.42	<0.0001	****	18	17

Table 16: Ordinary one-way ANOVA test for GFAP+ cells percentage. Summary of the test and p-value statistics of the ANOVA test and Tukey's multiple comparisons test.

Ordinary One-way ANOVA Test						
P value	<0.0001					
P value summary	****					
F	16.10					
R squared	0.36					
Tukey's multiple comparisons test						
Comparison	*Mean rank diff.*	*95% C.I.*	*Adjusted P*	*Summary*	*N1*	*N2*
0.03 kPa vs. 1.3 kPa	1.53	-5.6, 8.66	0.86	ns	24	19
0.03 kPa vs. 1000 kPa%	-15.29	-22.79, -7.79	<0.0001	****	24	16
1.3 kPa vs. 1000 kPa	-16.8	-24.71, -8.9	<0.0001	****	19	16

Table 17: Ordinary one-way ANOVA test for GFAP+ cell surface. Summary of the test and p-value statistics of the ANOVA test and Tukey's multiple comparisons test.

Ordinary One-way ANOVA Test						
P value	0.015					
P value summary	****					
F	4.52					
R squared	0.026					
Tukey's multiple comparisons test						
Comparison	*Mean rank diff.*	*95% C.I.*	*Adjusted P*	*Summary*	*N1*	*N2*
0.03 kPa vs. 1.3 kPa	71.41	8.01, 134.82	0.02	*	24	19
0.03 kPa vs. 1000 kPa%	64.20	-2.43, 130.83	0.06	ns	24	16
1.3 kPa vs. 1000 kPa	-7.21	-77.27, 62.83	>0.9999	ns	19	16

Table 18: Kruskal-Wallis test results for the average neurite lenght at DIV1. Test and p-value statistics of the Kruskal-Wallis and post-hoc Pairwise Mann-Whitney U test.

Kruskal-Wallis test				
P value	0.017			
Exact or approximate P value?	Approximate			
P value summary	****			
Kruskal-Wallis statistic	8.08			
Pairwise Mann-Whitney U test results				
Comparison	*Adjusted P Value*	*Summary*	*N1*	*N2*
0.03 kPa vs. 0.4 kPa	0.032	*	37	29
0.03 kPa vs. 1.3 kPa	0.08	ns	37	28
0.4 kPa vs. 1.3 kPa	>0.9999	ns	28	29